Vertical Structure and Kinematics of Tropical Monsoon Precipitation Observed from a 2875-MHZ Profiler During NAME

by
David G. Lerach

Department of Atmospheric Science
Colorado State University
Fort Collins, Colorado

Colorado State University

Department of Atmospheric Science

Paper No. 780

VERTICAL STRUCTURE AND KINEMATICS OF TROPICAL MONSOON PRECIPITATION OBSERVED FROM A 2875-MHZ PROFILER DURING NAME

Submitted by

David G. Lerach

Department of Atmospheric Science

In partial fulfillment of the requirements

For the Degree of Master of Science

Colorado State University

Fort Collins, CO

Fall 2006

ABSTRACT

VERTICAL STRUCTURE AND KINEMATICS OF TROPICAL MONSOON PRECIPITATION OBSERVED FROM A 2875-MHZ PROFILER DURING NAME

Deep cloud systems in the Tropics play a significant role in the global heat budget. This is due to the fact that atmospheric circulations, such as the Hadley and Walker cells, are sensitive to the shape of the diabatic heating profile, which in turn depends on the vertical structure of tropical convective systems. The goal of this project is to create a climatology of the vertical structure of precipitating cloud systems that characterized the 2004 North American monsoon. The study utilized data from the 2875-MHz profiler stationed near Sinaloa, Mexico from early July through mid-September of 2004 for the North American Monsoon Experiment (NAME).

The profiler observed 23 rain events. Climatologic frequency distributions of reflectivity, Doppler velocity, and spectral width were created for various precipitation regimes. The NAME distributions compared favorably with results from previous studies. Stratiform precipitation exhibited a radar bright band and a strong Doppler velocity gradient in the melting layer, and weak spectral width above the melting layer. Mixed stratiform/convective regions contained low reflectivity and a weak bright band. Convective profiles contained high reflectivity, large Doppler velocities, and high spectral width.

Vertical air motions derived from the 2875-MHz profiler were compared with EVAD and 449-MHz profiler retrievals. The 2875-MHz profiler vertical air motion estimates contained a negative bias to both methods of approximately 0.5 m s^{-1}. Though the errors in the stratiform vertical air motion estimates were of the same order as the stratiform air motions, the NAME vertical air motion composites for stratiform and mixed stratiform/convective precipitation exhibited similar features to composites from previous studies. However, convective composites from past studies showed ascent throughout the troposphere while the NAME composite showed a significant region of descent between 4 and 6 km. This discrepancy cannot be fully explained by the negative bias of 0.5 m s^{-1} in the NAME estimates.

Climatologic vertical profiles of precipitating clouds were successfully created from the 2875-MHz profiler NAME dataset for various precipitation regimes. While the vertical air motion estimates yielded unexpected values in the melting layer of convective precipitation, they proved useful in analyzing the vertical structure of vertical air motion for various precipitation regimes in a mean sense as well as assessing general updraft and downdraft intensity in individual convective cells.

David G. Lerach
Atmospheric Science Department
Colorado State University
Fort Collins, CO 80523
Fall 2006

ACKNOWLEDGEMENTS

I would like to thank my advisor, Dr. Steven Rutledge, for his guidance and continuous insight throughout this project. A special thanks goes to Dr. Christopher Williams of the University of Colorado and the Cooperative Institute for Research in Environmental Sciences (CIRES) for giving suggestions and supplying profiler data, as well as answering all of my questions regarding profiler radars. I am also grateful to Dr. Anthony Illingworth of the University of Reading, Reading, United Kingdom for his helpful suggestions. I want to extend my deepest appreciation to Drs. William Cotton and V. N. Bringi for their time given to this project. Sincere thanks go to past and current members of the CSU Radar Meteorology group, particularly Drs. Robert Cifelli, Steven Nesbitt, and Timothy Lang, as well as Paul Hein, Lee Nelson, Margi Cech, and Jillian L'Ecuyer for their support and insights for this work. Lastly, I would like to thank my family and friends for their encouragement over the years as I pursued a career in atmospheric science. This research was funded by the National Oceanic and Atmospheric Administration (NOAA) SHIP-NAME grant, grant number NA17RJ1228.

TABLE OF CONTENTS

LIST OF FIGURES

LIST OF TABLES

CHAPTER 1

Introduction

1.1 Background and Motivation

One of the greatest challenges in atmospheric numerical modeling is the realistic simulation of the hydrologic cycle. This requires proper specifications of realistic distributions of diabatic heating, important for the forcing of atmospheric circulations over a broad range of scales (Williams et al. 1995). In particular, deep cloud systems in the Tropics are thought to play a significant role in the global heat budget (e.g., Ackerman et al. 1988; Lubin et al. 1996), because the release of latent heat in tropical convective systems drives the Hadley and Walker circulations. The vertical distribution of diabatic heating depends on the vertical structure of these convective systems and is very different for mature stratiform-dominated systems than for classical deep convective towers. Atmospheric circulations are sensitive to the shape of the diabatic heating profile (Hartmann et al. 1984). It is therefore necessary to develop global climatologies of the structure of precipitating cloud systems to improve the parameterization of atmospheric heating due to the release of latent heat in precipitating cloud systems (Johnson 1984; Houze 1989), especially in the Tropics (Williams et al. 1995; Ecklund et al. 1999).

A recent geographical focal point of atmospheric research and modeling has been that of the North American monsoon (NAM). The core of this region includes Baja,

California, the Gulf of California, southwestern United States, and western Mexico, including the western flanks of the Sierra Madre Occidental (SMO) (Figure 1.1). The combination of these seasonally warm land surfaces in lowlands and elevated areas together with atmospheric moisture supplied by the Gulf of California is conducive to the formation of the NAM system (Adams et al. 1997). This warm-season rainfall is responsible for most of the annual precipitation in southwestern North America. Most of the region receives over 50 % of its annual precipitation in July, August, and September. Figure 1.2 shows the seasonal distribution of precipitation for various sites across southwestern North America. The regional streamflow regime becomes increasingly dependent on this warm-season precipitation as one travels southward into western Mexico (Gochis et al. 2003), a transition signifying the importance of rainfall generated by the NAM system to local and regional water resources. Seasonal variability in this rainfall is of practical concern for watershed managers, ranchers, and planners of southwestern North America (Adams et al. 1997).

The semiarid climate of the NAM region presents unique weather and climate forecasting challenges, and recent years have seen an increased interest in diagnosing and modeling the physical processes controlling the regional climate and its associated modes of variability, both seasonal and inter-annual (Gochis et al. 2004). Therefore, it would be beneficial to create a climatology of the vertical structure of NAM precipitation to aid in better understanding the effects these warm-season tropical convective systems have on the larger scale circulation through latent heat release.

1.2 NAME Overview

The North American Monsoon Experiment (NAME) took place during the summer and early fall of 2004 within the core region of the North American monsoon, primarily northwestern Mexico, southwestern United States, and adjacent ocean areas (Tier-I domain). Figure 1.3 depicts the multi-tiered regions of the NAME domain. The focus of the field campaign was to improve predictability of warm-season precipitation over North America by analyzing numerous atmospheric, oceanic, and land surface factors including the Gulf of California low-level jet and moisture surges, easterly wave and tropical cyclone influences, monsoon onset, mesoscale convective systems, and topographical effects. The effort utilized over 20 different instrument platforms, including the NCAR S-Pol polarimetric Doppler radar, the NOAA 2875-MHz, 915-MHz, and 449-MHz vertically pointing profiler radars, satellites, research vessels and aircraft, surface meteorological stations, rain gauge networks, and disdrometers (Higgins et al. 2006).

The core North American Monsoon precipitation regime within the NAME Tier-I region can be characterized as a diurnally modulated convective regime that is forced by intense heating of topography inland of a large body of water (Gochis et al. 2004). A main consideration during NAME was how convective systems and regional circulations in the Tier-I domain vary over the warm-season diurnal cycle. Precipitation feature analyses were performed with the S-Pol radar for the NAME dataset. The work revealed that mesoscale convective systems (MCSs) are the dominant mode of convection in the region. The systems grow upscale from smaller convection that develops in the afternoon over the SMO, which can lead to MCS activity during the evening hours. There is also a

secondary maximum of MCS precipitation in the morning hours where systems develop along the land breeze near the coast (Lang et al. 2005).

1.3 Scientific Objectives and Organization of Paper

During the North American Monsoon Experiment (NAME) in 2004, two vertically pointing profiler-radars were placed at the NOAA Environmental Technology Laboratory (ETL) / Aeronomy Laboratory (AL) meteorological super site in Sinaloa, Mexico from early July through mid-September to measure the microphysical properties of tropical monsoon rainfall (i.e., the drop size distribution). The 449-MHz profiler scanned from the surface to the melting layer (approximately 4.5 km) while the 2875-MHz profiler probed the lower 15 km of the atmosphere. The site was situated approximately 45 km north-northwest of the S-Pol radar location, allowing for coordinated profiler and scanning radar analyses. Figure 1.4 gives the locations of the S-Pol radar and the NOAA super site within the NAME Tier-I region. The NOAA profiler site instrumentation sampled monsoon onset, the diurnal cycle of convection, land and sea breezes, and both easterly wave and tropical cyclone influences. More than 150 hours of data were recorded from the 23 rain events that passed over the site. This study uses data from the S-Pol and profiler radars deployed during NAME to track specific MCSs in time and space to examine them in the context of their individual life cycles and diurnal cycles, kinematics, and microphysical structure. Utilizing the entire dataset to create climatologic profiles of precipitation, this study also investigates the mean vertical structure and kinematics of the precipitating cloud systems that characterized the 2004 North American monsoon.

This paper is organized into four chapters. The data and instrumentation platforms used in this work, including a description of the S-Pol polarimetric radar variables, will be discussed in the first section of chapter 2. The later sections will describe the various methodologies used in the study. Two case studies as well as the climatology of all 23 profiler events will be examined in chapter 3. In chapter 4 conclusions will be drawn from this study, and future work will be proposed.

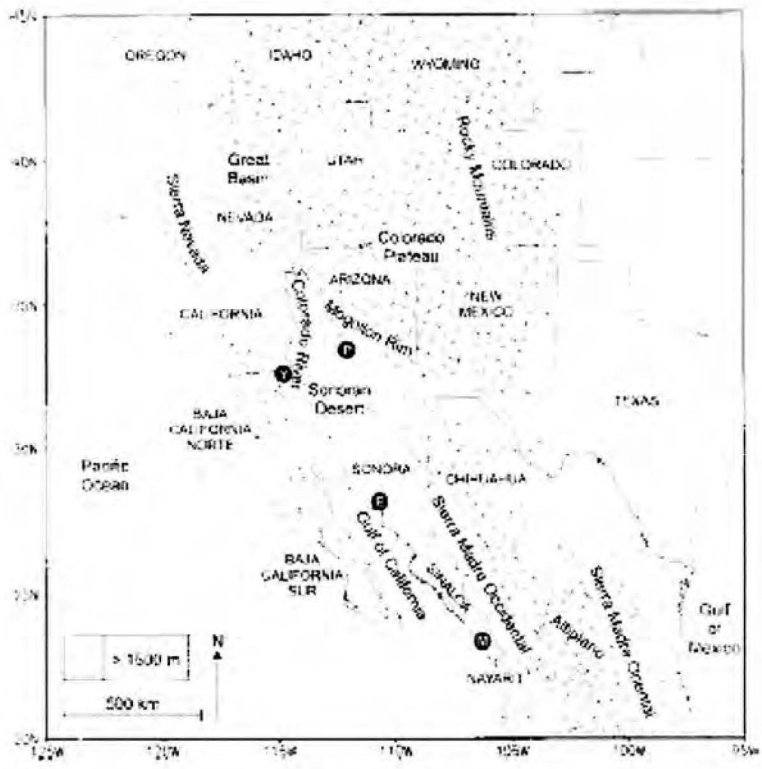

Figure 1.1: The core region of the North American Monsoon. Terrain greater than 1500 m are identified with "inverted v" symbols. Key areas of interest include Baja, the Gulf of California, and the Sierra Madre Occidental mountain range. The cities of Sinaloa and Mazatlán (M) are labeled (from Adams et al. 1997).

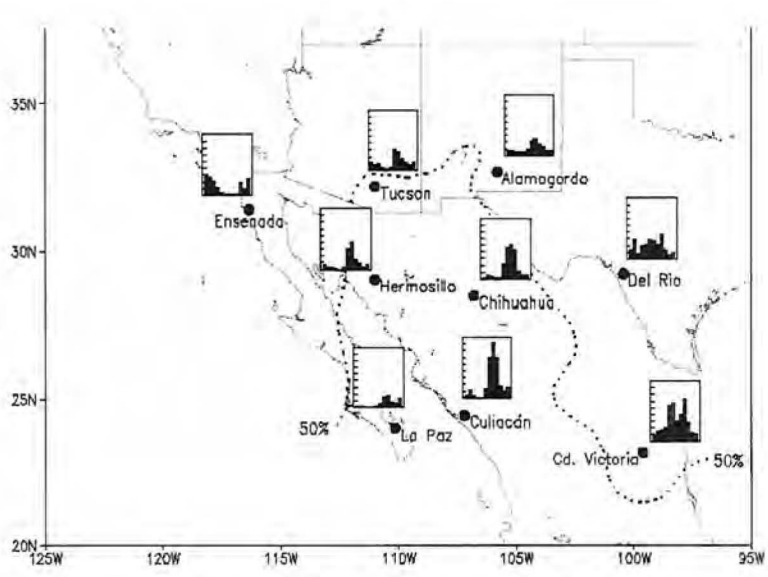

Figure 1.2: Seasonal distribution of precipitation for southwestern North America. The largest peaks in mid-to-late summer rainfall are found in northwestern Mexico. Areas south of the dashed line receive at least 50 % of their annual rainfall during July, August and September (after Douglas et al. 1993).

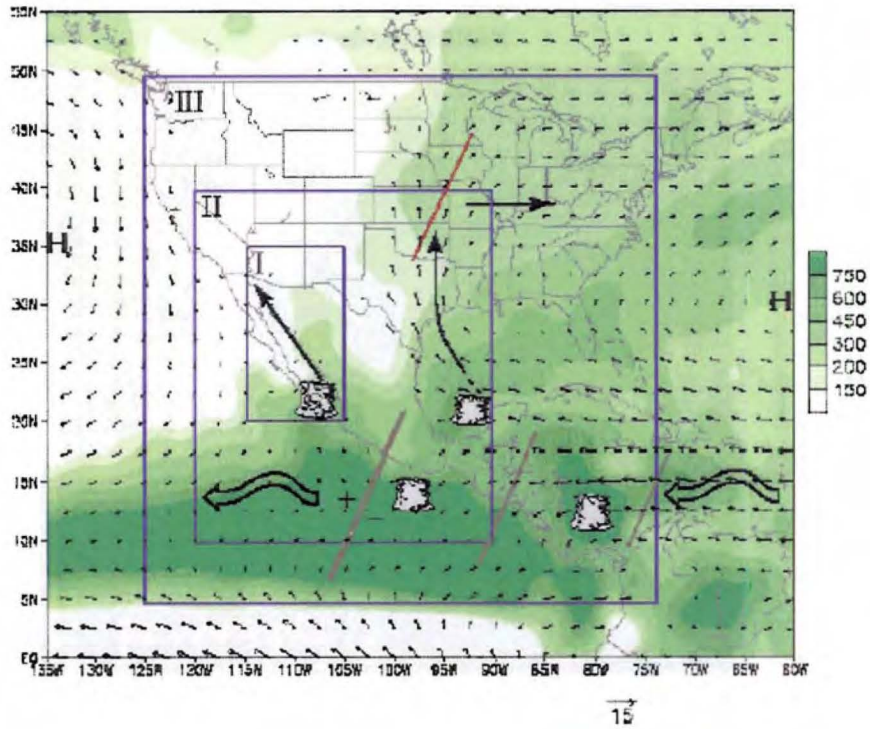

Figure 1.3: Schematic illustrating the multi-tiered approach of NAME. The schematic also shows mean (July–September 1979–95) 925-hPa wind vectors (ms^{-1}) and merged satellite estimates and rain gauge observations of precipitation (shading) in millimeters. Circulation data are taken from the NCEP–NCAR Reanalysis archive. The Gulf of California (Great Plains) low-level jet is indicated by the straight (curved) arrow in the GOC (southern plains). The schematic includes transient lines near 10°–15°N (40°N) to indicate westward (eastward) propagation of disturbances such as easterly waves (from Higgins et al. 2006).

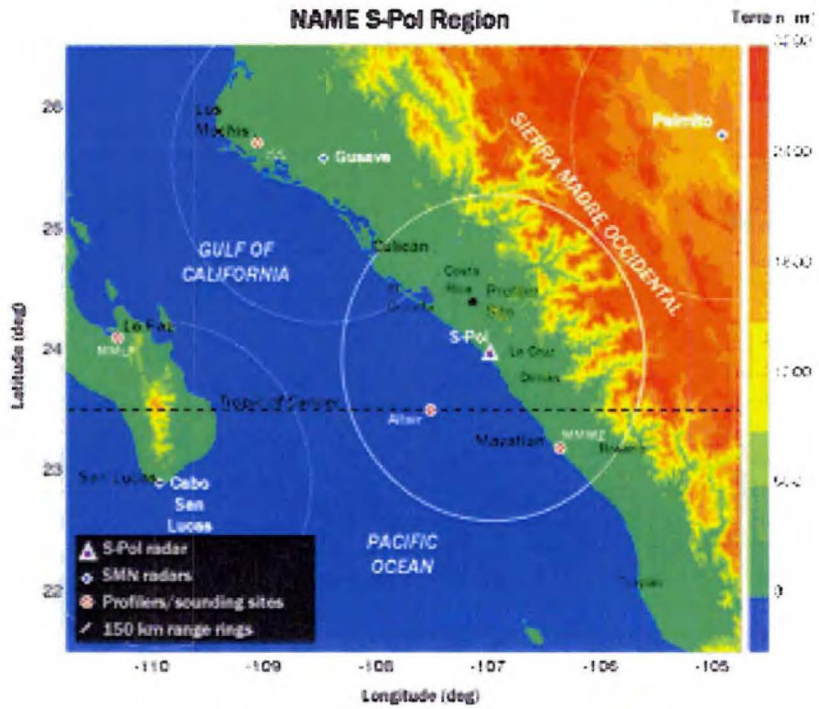

Figure 1.4: Schematic of the NAME S-Pol radar location. The S-Pol radar was located just west of La Cruz, Mexico while the NOAA super site (profiler site) was placed roughly 45 km to the northwest in Sinaloa. The SMN radars are also marked with diamonds. The white circles indicate the various radar maximum range rings. The terrain is also contoured in meters (from Williams et al. 2006).

CHAPTER 2

Data and Methodology

2.1 NAME: Data and Observational Platforms

2.1.1 S-Pol Polarimetric Doppler Radar

Radars have been used for meteorological purposes since World War II. Today's radars operate at various wavelengths and utilize multiple scanning techniques to study clouds, precipitation, particle types, and even turbulent air motions in the planetary boundary layer (Houze 1993). This study uses data collected by the NCAR polarimetric Doppler radar (S-Pol) operating at S-band (~ 3 GHz, or 10 cm). During NAME, S-Pol was placed near La Cruz, Mexico. The radar provided both kinematic and microphysical information about the precipitation that moved over the NAME Tier-I domain from early July through mid-August.

Polarimetric radars, such as S-Pol, can transmit and receive both horizontal and vertical polarizations of electromagnetic waves. A horizontally- and vertically-polarized electromagnetic wave is illustrated in Figure 2.1. S-Pol has the ability to transmit the horizontal and vertical pulses alternately or simultaneously. During NAME, the alternate transmission mode was used, allowing for the retrieval of the cross-polar signal, or the signal returned in the polarization orthogonal to that which was transmitted. The co-polar signal is when the received and transmitted signals have the same polarization. In sections 2.1.1.3-7, the subscripts h and v will refer to the horizontal and vertical

polarizations, respectively. The first subscript will denote the polarization of the transmitted wave, while the second will indicate that of the received wave. This section will discuss the S-Pol radar variables and how they can be used in bulk hydrometeor identification retrieval.

2.1.1.1 Reflectivity, Z_h

The reflectivity factor (Z) is a measure of the total transmitted power backscattered to the radar from the particles in a radar volume. If the particles are spherical and sufficiently small compared to the wavelength of the radar ($D < 0.07\ \lambda$), conditions for the Rayleigh approximation are satisfied. In this case, the reflectivity factor can be written as (Eqn. 2.1):

$$Z = \int_0^\infty N(D) D^6 dD \qquad [\mathrm{mm^6\,m^{-3}}] \qquad (2.1)$$

where D (mm) is the diameter of the particles and N(D) is the concentration of particles with diameter D. Z can be measured for both horizontally- and vertically-polarized electromagnetic waves, however this study primarily uses the horizontally polarized reflectivity factor (Z_h). Z is proportional to the sixth moment of the particle diameter, meaning that larger particles produce significantly larger reflectivity values than smaller particles. Values of Z can span several orders of magnitude, so radar reflectivity is expressed using a logarithmic scale (Eqn. 2.2):

$$Z_h = 10 \log_{10} Z \qquad [\mathrm{dBZ}] \qquad (2.2)$$

In terms of meteorological targets (i.e. water and ice), this scale ranges from values near zero in cumulus clouds to values greater than 60 dBZ in intense rain or hail (Doviak and Zrnić 1993).

2.1.1.2 Radial Velocity, V_r

The radial velocity (V_r) is a measure of the mean (power-weighted) velocity of particles in a given radar volume in the radial direction (motion towards/inbound or away/outbound from the radar). Pulsed Doppler radars can detect very small modulations of the radar frequency from returned electromagnetic pulses, called the Doppler shift. The radial velocity relates to the Doppler shift frequency (f) by Eqn. 2.3:

$$f = 2\frac{V_r}{\lambda} \qquad [s^{-1}] \qquad (2.3)$$

V_r is expressed in units of ms^{-1} and λ in m.

The maximum unambiguous velocity measurable by the radar is called the Nyquist velocity (v_{max}). The Nyquist velocity is a function of the pulse repetition frequency, or PRF (Rinehart 2004). Their relationship is given by Eqn. 2.4:

$$v_{max} = \pm PRF\frac{\lambda}{4} \qquad [m\ s^{-1}] \qquad (2.4)$$

Velocities greater than the Nyquist velocity are referred to as "folded." Folding must be accounted for in Doppler velocity data processing. A full description of Doppler radar techniques to calculate radial velocity is presented in Doviak and Zrnić (1993) and Bringi and Chandrasekar (2001).

2.1.1.3 Differential Reflectivity, Z_{dr}

The differential reflectivity (Z_{dr}) can be expressed as the ratio of the horizontal reflectivity factor to the vertical reflectivity factor (Eqn. 2.5):

$$Z_{dr} = 10\log_{10}\left(\frac{Z_{hh}}{Z_{vv}}\right) \qquad \text{[dB]} \qquad (2.5)$$

Z_{dr} provides a measure of particle shape (or oblateness) and is useful for distinguishing hail from rain. Due to the combined effects of gravity, surface tension, and aerodynamic forces on a falling raindrop (D > 1 mm), it will exhibit the shape of an oblate spheroid with the maximum dimension aligned in the horizontal direction (Pruppacher and Beard 1970; Beard and Chuang 1987). Figure 2.2 shows the evolution of drop oblateness with increasing diameter. Thus, for rain, larger positive values of Z_{dr} correspond to larger drops. Ice behaves very differently than rain due to its more rigid shape and reduced dielectric constant. Spherical or tumbling hail takes on values of Z_{dr} near 0 dB. The presence of vertically aligned ice will lead to negative Z_{dr} values. Figure 2.3 presents various curves of Z_{dr} as functions of axis ratio and hydrometeor type.

2.1.1.4 Linear Depolarization Ratio, LDR

The linear depolarization ratio (LDR) is defined as the ratio of the cross-polar returned power signal to the co-polar returned power signal (Eqn. 2.6):

$$LDR = 10\log_{10}\left(\frac{Z_{hv}}{Z_{hh}}\right) \qquad \text{[dB]} \qquad (2.6)$$

LDR is a measure of particle shape, canting angle, and phase of the hydrometeors in the radar volume. Particles with an oblate shape tend to wobble as they fall, resulting in a wide assortment of canting angles. LDR increases with increasing dielectric strength,

more irregular shapes, and increasing axis ratio. Figure 2.4 plots various curves of LDR as functions of axis ratio and ice particle type. LDR values of rain are approximately –30 dB, snowflakes are near –32 dB, and oblate dry hail or graupel is around –20 dB (Doviak and Zrnić 1993). Wet aggregates and wet hail exhibit LDR values greater than –20 dB due to their irregular shapes and wet surfaces. For particles with their major or minor axes aligned with the incident electric field there will be no cross-pole return and LDR values will approach negative infinity. It should be noted that LDR is susceptible to more noise contamination than some of the other radar variables because the cross-polar power returned is near two orders of magnitude below the co-polar signal (Doviak and Zrnić 1993).

2.1.1.5 Correlation Coefficient, ρ_{hv}

The correlation coefficient at zero lag, $\rho_{hv}(0)$ (hereafter, ρ_{hv}), is the statistical correlation of the co-polar received power in the horizontal polarization to the co-polar received power in the vertical polarization (Eqn. 2.7):

$$\rho_{hv} = \frac{|\langle S_{vv} S_{hh} \rangle|}{\left(\langle |S_{hh}|^2 \rangle \langle |S_{vv}|^2 \rangle\right)^{1/2}} \tag{2.7}$$

where $|\langle S_{hh} S_{vv} \rangle|$ is the magnitude of the average of the co-polar powers and $\langle |S_{hh}|^2 \rangle$ and $\langle |S_{vv}|^2 \rangle$ are the average squares of the magnitude of the co-polar powers. The horizontal and vertical pulses are said to have zero lag time, because it is assumed they have transmitted simultaneously. ρ_{hv} can be reduced by particle shape, size, canting angles, eccentricity, shape irregularities, hydrometeor type and mixture (concentration of water vs. ice), and the differential phase shift upon scattering (Doviak and Zrnić 1993). Noise

can also reduce the correlation between pulses (Rinehart 2004). ρ_{hv} is mainly an indicator of the variability of hydrometeor types within a radar volume. Values for pure drizzle are near unity (> 0.98) while more intense rainfall is still greater than 0.95. The correlation coefficient decreases in mixed-phase situations because the distribution of sizes, shapes, phase and canting angles broaden as the ice particle size increases (Zrnić et al. 1993; Carey and Rutledge 1996). Rain-hail mixtures tend to have ρ_{hv} values near 0.9, and rain-snow mixtures (i.e., the melting layer) can take on values around 0.8. Values in meteorological echo rarely fall below 0.8, making ρ_{hv} a useful variable for discriminating between meteorological and non-meteorological targets.

2.1.1.6 Differential Propagation Phase, Φ_{dp}, and Specific Differential Phase, K_{dp}

When a radar-transmitted electromagnetic wave propagates through an oblate raindrop, it is slowed down slightly. However, due to particle oblateness, the wave will be slowed more for the horizontal polarization than for the vertical, eventually leading to a time (phase) lag between the two polarization states. This produces a slight change in phase between the two signals called the differential propagation phase, or simply differential phase, Φ_{dp} (Rinehart 2004). The radar directly measures the total differential phase shift (Ψ_{dp}), which is the sum of the propagation effects (Φ_{dp}) and the differential backscatter phase, δ (Eqn. 2.8):

$$\Psi_{dp} = \Phi_{dp} + \delta \qquad \text{[deg]} \qquad (2.8)$$

At S-band, when Rayleigh conditions apply, δ is zero, in which case the total differential phase is due to propagation effects alone (i.e., $\Psi_{dp} = \Phi_{dp}$). Oblate particles, such as large raindrops, will result in a positive phase shift. Prolate particles, such as vertically aligned

ice (in an electric field for example) will result in a negative phase shift. Isotropic hydrometeors, such as hail, will shift the phase equally in both polarizations, resulting in no differential phase shift. The filtering of Φ_{dp} with range is necessary to reduce the high degree of variability often observed with this variable (Hubbert and Bringi 1995).

The specific differential phase (K_{dp}) for a volume is calculated from the range derivative of Φ_{dp} using a finite difference scheme (Eqn. 2.9).

$$K_{dp} = \frac{1}{2}\frac{\delta\Phi_{dp}}{\delta r} = \frac{|\Phi_{dp}(r_2) - \Phi_{dp}(r_1)|}{2(r_2 - r_1)} \qquad [\text{deg km}^{-1}] \qquad (2.9)$$

where r is the range to the target from the radar in km, and the factor of two accounts for the two-way propagation distance. K_{dp} is affected only by anisotropic scatterers (oblate raindrops) and is proportional to the liquid water content and mean oblateness in a radar volume. Therefore, K_{dp} can be used to discriminate between rain and hail in a mixed phase environment and often allows for more accurate rainfall estimations, especially in high rainfall rates (Jameson 1985; Chandrasekar et al. 1990).

2.1.1.7 Bulk Hydrometeor Identification Using Fuzzy Logic

The microphysical characteristics of hydrometeors lead to differences in the scattering and propagation of polarized waves that are manifested in the polarimetric radar variables. Thus, these variables yield information about the particle size, particle shape, phase, density, and particle orientation of hydrometeors in a bulk sense. Liu and Chandrasekar (2000) described a fuzzy logic system that allows for hydrometeor type classification based on overlapping and "noise contaminated" polarimetric radar data.

Fuzzy logic is a process of four steps: 1) fuzzification, 2) inference, 3) aggregation, and 4) defuzzification. During fuzzification, each radar variable

measurement (Z_h, Z_{dr}, LDR, etc.) is converted into a truth value for each hydrometeor type ranging from 0 to 1. This is called a fuzzy set. A truth value of 1 indicates that the particular value of that radar variable uniquely identifies the hydrometeor type in question. One specific input value can belong to several fuzzy sets with different truth values. A membership beta function describes the relationship of the measured value to a fuzzy set. An example of a membership beta function for Z_h for mid-latitude summer storms is shown in Figure 2.5. Based on this example, if there is a Z_h measurement of 20 dBZ, the bulk hydrometeor type that corresponds to that measurement can only be drizzle, low-density dry ice, or high-density dry ice. Once every truth value is assigned, the inference step combines the truth value for each variable to determine a net truth value for each hydrometeor type. During the aggregation step, the maximum truth value is determined. The defuzzification step refers to the conversion of that truth value into a single hydrometeor type that is best described by the fuzzy output set (Liu and Chandrasekar 2000). It should be noted that while there is likely more than one type of hydrometeor in any given radar volume, this method chooses the single hydrometeor species that dominates the return. Zrnić et al. (2001) note that since some variables may be more reliable than others, a weighting scheme can be employed to minimize the effects of bogus and noisy data. Table 2.1 lists typical values of various polarimetric radar variables for different hydrometeor types in tropical rainfall. See Liu and Chandrasekar (2000) for a complete explanation on hydrometeor identification using fuzzy logic.

This study utilized one dimensional membership functions for eleven hydrometeor types: drizzle, rain, wet snow, dry snow, low density (or 'dry') graupel, high

density (or 'wet') graupel, small hail, large hail, small hail mixed with rain, large hail mixed with rain, and vertically aligned ice. The input variables were, Z_h, Z_{dr}, K_{dp}, LDR, ρ_{hv}, and temperature. Fuzzy logic-based hydrometeor identification from S-Pol aided in the creation of a simplified HID algorithm that only required variables measured by the 2875-MHz profiler. The algorithm is discussed in section 2.2.2.

2.1.1.8 Data Processing

The S-Pol NAME dataset was corrected for attenuation, clutter, insect, and second-trip contamination. The rainfall attenuation correction methodology was based off Carey et al. (2000). Non-meteorological echo was removed via thresholds on various polarimetric fields, including reflectivity, Z_{dr}, and Φ_{dp}. A combination of thresholds on LDR and Φ_{dp} was used to remove second-trip echo. Remaining clutter and insect echo were removed by hand with the NCAR SOLO (version II) software package. The data was then despeckled using the soloii algorithm, removing any echo that contained two or fewer contiguous gates (Lang et al. 2005). Significant beam blockage occurred in S-Pol's northeast sector (351-105° azimuth) caused by terrain peaks intercepting the radar beam at low elevation angles. This blockage was corrected by the examination of the behavior of Z_h as a function of azimuth for a given range of K_{dp}. See Lang et al. (2005) for a complete description of this method.

Φ_{dp} was filtered using a 21-gate (3.15-km; 150-m gate spacing) finite impulse response filter developed by Dr. V. N. Bringi of Colorado State University. K_{dp} was calculated from the slope of the line fitted to the filtered Φ_{dp} field. The window over

which this line was fitted changed depending on the Z_h of the central gate (Lang et al. 2005).

2.1.2 NOAA 2875-MHz Profiler

This study utilizes high-resolution data collected by the NOAA 2875-MHz (S-band) profiler radar. The vertically pointing Doppler radar uses profiler technology and a fixed dish antenna. The precipitation profiler is sensitive primarily to Rayleigh scattering processes, and measures equivalent reflectivity, Doppler velocity, and spectral width. Equivalent reflectivity is the concentration of uniformly distributed water particles that would return the amount of back-scattered power received, expressed in units of dBZ (Rinehart 2004). Spectral width is simply the standard deviation of the velocity spectrum (Rinehart 2004). The radar provides detailed profiles of the vertical structure of overhead precipitation with 45-second temporal resolution (15 s per mode). The NOAA profiler operates in three modes: high-resolution, or precipitation mode, attenuated mode, and cloud mode. These modes are characterized by the different radar transmitted pulse lengths and by the attenuation in the radar circuitry (Williams et al. 2006). Precipitation mode uses a pulse length of 60 m to maintain high vertical resolution and is used for looking at hydrometeors. This mode saturates at high reflectivity. The attenuated mode uses the same operating parameters as precipitation mode but with an additional attenuator to provide measurements when precipitation mode is saturated in low level, high reflectivity precipitation. The cloud mode uses a longer pulse length of 105 m and is pulse coded to improve sensitivity to low-reflectivity clouds. Note that the width of the profiler beam broadens with range (height), and thus so does

the pulse volume, which is a function of the beam width and pulse length. This means that measurements further from the profiler are based on the sampling of targets in a larger domain (Rinehart 2004). The 2875-MHz profiler beam broadening with range (height) is illustrated in Figure 2.6 (blue curve).

The 2875-MHz profiler was stationed at the NOAA super site in Sinaloa, Mexico (24.48° N, 107.16° S) roughly 45 km northwest of the S-Pol location and operated from 30 July to 18 September during NAME. The reflectivity was calibrated by comparing the profiler observations with simultaneous S-Pol observations over the profiler site. See Williams et al. (2006) for a complete description of the procedure. This study uses the dataset collected in precipitation mode.

2.1.3 NOAA 449-MHz Profiler

This study also utilizes a low-level dataset from the NOAA 449-MHz profiler radar. The profiler uses a co-linear co-axial antenna, composed of dipole elements encased in a fiberglass tube. At 449-MHz, the profiler is sensitive to both Rayleigh scattering and scattering of energy from the irregularities in the refractive index due to turbulence (Bragg scattering). Radar observables include backscattered power, Doppler velocity, spectral width, and horizontal winds using the Doppler Beam Swinging (DBS) method. Operations consist of two scanning modes: 1) vertical mode and 2) DBS mode. The vertical mode uses only a vertical beam while the DBS mode scans with three radar beams in the North, vertical, and East directions. Both modes have 250-meter vertical and 40-second temporal resolution (Williams et al. 2006). The broadening of the 449-MHz profiler's beam with height is also plotted in Figure 2.6 (red curve).

The 449-MHz profiling radar was placed at the NOAA super site to primarily measure the horizontal winds and vertical air motions in the lower troposphere. The radar collected data from late July to mid-September during NAME. The reflectivity was calibrated to the 2875-MHz profiler by comparing simultaneous reflectivity spectral densities observed in the vertical beams. The gain of the 449-MHz profiler was adjusted until the Rayleigh scattering portion of the spectra agreed between the two radars (Williams et al. 2006). This study utilized 449-MHz profiler vertical air motion data for the 31 July and 13 August 2004 rainfall events.

2.2 Vertical Air Motion Retrieval

One focus of this project was to estimate the vertical air motion with the NOAA 2875-MHz profiler for the NAME dataset without losing the profiler's vertical or temporal resolution. Retrieving vertical air motion from an S-band vertically pointing Doppler radar requires calculating the hydrometeor terminal fall speeds. This means the bright band must be accounted for in the reflectivity measurements and a relatively accurate technique for hydrometeor identification must be applied. The following section describes the methodology used in this project to perform vertical air motion retrievals on the NAME 2875-MHz profiler dataset.

2.2.1 Bright Band Filter

When snow melts to form rain as it falls through the melting layer, the cross-section of the hydrometeors is enhanced at S-band wavelengths. This results in a higher power returned to the radar, and thus, a higher reflectivity measurement than if there were

only raindrops or only snow. This enhanced reflectivity in the melting layer, often visible on radar displays of stratiform precipitation, is called the radar bright band (Cheng and Collier 1993). If uncorrected, a reflectivity-biased hydrometeor identification (HID) algorithm, such as the one used in this study (section 2.2.2), would likely choose the wrong hydrometeor species associated with the bright band measurements. A simple bright band reflectivity interpolation scheme was implemented for the NAME profiler dataset to solve this dilemma.

The scheme is applied to the dataset at each time period (a single profile at a time). It first decides whether or not the profile contains precipitation (real data values). If so, the mean reflectivity is calculated for three regions: the lowest 3.5 km, the 5.5 – 7.5 km layer, and the melting layer (3.5 – 5.5 km). The melting layer mean reflectivity is computed from only the three largest reflectivity values in the layer. Both the vertical and horizontal (time-based) reflectivity gradients are computed throughout the melting layer as well. For the algorithm to declare a profile to be bright band-contaminated, three criteria must be satisfied: 1) the mean melting layer reflectivity must be greater than the mean reflectivity values of both the 0 – 3.5 km and 5.5 – 7.5 km layers 2) the vertical reflectivity gradient must be large near both boundaries of the melting layer 3) the horizontal reflectivity gradient must be relatively weak through most of the melting layer. If a profile is deemed to contain a bright band presence, the reflectivity values within the bright band are linearly interpolated from the reflectivity just outside (above and below) of the region. Once every profile has undergone this process, a quality check is performed where each profile is reevaluated. If a profile is originally marked as containing radar bright band and surrounded by profiles that are not, it is no longer

classified as having a bright band and is given back its original melting layer reflectivity values. When this process finishes, a smoothing technique is applied. Every value that has been identified as containing a bright band presence is averaged in time by ± 45 s (± 1 time gate).

The bright band reflectivity interpolation scheme performed with remarkable accuracy, successfully filtering out the radar bright band in all 23 profiler events. Figure 2.7 depicts the algorithm-corrected reflectivity in a time vs. height contour plot for the (a) 31 July and (b) 13 August rain events. The algorithm's performance allowed for accurate hydrometeor identification retrieval.

2.2.2 Simplified Hydrometeor Identification Technique

The S-Pol radar observed many of the same precipitation events as the S-band profiler. The profiler scanned in precipitation mode every 45 seconds with 60-meter vertical resolution while S-Pol scanned in its surveillance mode (Lang et al. 2005) approximately every 10 minutes with relatively poor vertical resolution (> 1 km resolution at 7 km). Given this reduced resolution, it was decided not to perform hydrometeor identification over the profiler site using the S-Pol polarimetric variables and fuzzy logic-based method. Instead, a more simplistic hydrometeor identification look-up table was developed for NAME based only on temperature and S-band profiler reflectivity. This allowed the study to preserve the high vertical and temporal resolution of the profiler data.

To create the simplified HID algorithm, a basic template for the look-up table was first produced based on general reflectivity- and temperature-hydrometeor type

relationships for tropical rainfall given by May and Keenan (2005) (Table 2.1). The look-up table was then 'tuned' to the S-Pol fuzzy logic scheme by forcing it to best represent the S-Pol RHI (see Rinehart 2004) fuzzy logic NAME dataset. The RHI scans provided better vertical resolution than the surveillance scans. The final simplified HID look-up table is shown in Table 2.2. Hydrometeor species given from the table include, drizzle, rain, dry snow, wet snow (melting layer), dry graupel, wet graupel, hail, and rain-hail mixtures. The algorithm proved to be effective, matching the S-Pol fuzzy logic output 95 % of the time. An example of the look-up table's performance to that of the fuzzy logic scheme is illustrated in Figure 2.8.

2.2.3 Precipitation Regime Classification

The vertical distribution of diabatic heating in convective systems depends on the vertical structure of precipitation in those systems. Therefore, a goal of this project was to develop climatologic profiles of various precipitation regimes during NAME. This required separating the individual S-band profiles into different precipitation regime classifications.

The precipitation regime classification algorithm created for this study is modeled after the algorithm from Williams et al. (1995). It has four classifications: 1) stratiform 2) convective 3) mixed stratiform/convective and 4) non-precipitating lofted clouds, or cirrus. The algorithm consists of a hierarchy of classification choices, beginning with general requirements and progressing towards more specific prerequisites. Each classification option is considered to be of higher precedence than all options given before it. This format allows for the classification of nearly every data profile. The

classification algorithm is described in Figure 2.9. After all profiles are initially classified, they are quality-checked using another hierarchy technique. This quality check consists of four loops. First, all random profiles originally classified as non-convective that are surrounded by convective profiles are reclassified as convective. Next, all random profiles originally classified as non-mixed that are surrounded by mixed profiles are reclassified as mixed stratiform/convective. Third, all random profiles originally classified as non-cirrus that are surrounded by cirrus profiles are reclassified as cirrus. Finally, all random profiles originally classified as non-stratiform that are surrounded by stratiform profiles are reclassified as stratiform. The algorithm was very effective. Less than 30 minutes of the entire profiler dataset had to be manually reclassified due to misclassification by the algorithm. Figure 2.10 depicts the algorithm's performance for the 31 July 2004 profiler event.

2.2.4 Hydrometeor Terminal Fall Speed and Vertical Air Motion

For an S-band vertically pointing profiler radar, the measured Doppler velocity spectrum is the convolution of the fall velocity spectra associated with the hydrometeor size distribution and the vertical air motion spectrum (Williams et al. 1995). This relationship can be written as (Eqn. 2.10):

$$V_d = w - V_t \qquad [\mathrm{m\ s^{-1}}] \qquad (2.10)$$

where V_d is the measured Doppler velocity in the vertical direction (positive upward), w is the vertical air motion (positive upward), and V_t is the terminal fall velocity of the hydrometeors (positive downward) (Rogers 1964; Williams et al. 1995). The NOAA profiler measured the Doppler velocity spectra for the 23 events during NAME. To

estimate the associated vertical air motions with the same resolution, the hydrometeor terminal fall speeds had to be approximated as accurately as possible. Once this was accomplished, the presence of the hydrometeor fall speeds was extracted from the Doppler velocity spectra, yielding the vertical air motion estimates.

Fall velocity calculations in regions designated as drizzle and rain were based on a manually derived V_t-Z relationship. Reflectivity, as measured by a Doppler radar, is defined in Eqn. 2.2. Assuming a normalized gamma drop size distribution (DSD), the number concentration, N(D) can be expressed as (Eqn. 2.11):

$$N(D) = N_w f(\mu)\left(\frac{D}{D_o}\right)^{\mu} \exp\left[-(3.67+\mu)\frac{D}{D_o}\right] \qquad [\mathrm{m}^{-4}] \qquad (2.11)$$

where D (m) is the drop diameter, N_w (m^{-4}) is the normalized slope intercept, D_o (m) is the median volume diameter, μ is the shape parameter, and $f(\mu)$ is shorthand for Eqn. 2.12 (Bringi and Chandrasekar 2001):

$$f(\mu) = \frac{6}{3.67^4}\frac{(3.67+\mu)^{\mu+4}}{\Gamma(\mu+4)} \qquad (2.12)$$

The reflectivity then becomes (Eqn. 2.13):

$$Z = N_w f(\mu)\Gamma(\mu+7)\frac{D_o^{\,7}}{(3.67+\mu)^{\mu+7}} \qquad [\mathrm{m}^3] \qquad (2.13)$$

In this form, Z becomes a function of N_w, μ, and D_o. If N_w and μ are assumed to be constant (independent of D), D_o is the only unsolved variable. Substituting the known relationship between D_o and V_t (Table 2.3) leads to a relationship between Z and V_t.

The parameters N_w and μ were derived from the 449-MHz and 2875-MHz profiler datasets for 13 August 2004 and provided by Dr. Christopher Williams of CIRES. These parameters were derived in the lowest 4 km (rain only). For a description of the

procedure used to create these parameters, see Williams et al. (2006). The quality-controlled mean value of N_w was determined to be 1000 mm^{-1} m^{-3}. The mean value of μ was 10. These values were used to create the V_t-Z relationship utilized in this study. Once V_t was calculated for values of reflectivity corresponding to D_o values ranging from 0.4 to 3 mm, a sixth order polynomial was fit to the data (Eqn. 2.14):

$$V_t = 1.895e-10Z^6 - 2.573e-8Z^5 + 8.777e-7Z^4$$

$$-1.339e-5Z^3 + 6.907e-4Z^2 + 0.099Z + 3.246 \qquad [\text{m s}^{-1}] \qquad (2.14)$$

where Z is in units of dBZ. This relationship is plotted in Figure 2.11. It is interesting to note that Joss and Waldvogel (1970) created an observation-based V_t-Z power-law relationship for rain. When compared to various normalized gamma DSD-based V_t-Z relations, the observation-based equation fit best to the gamma distribution which assumed N_w equal to 8000 mm^{-1} m^{-3} and μ equal to 5, values corresponding to a Marshall-Palmer like distribution. This suggests that NAM rainfall statistics assuming the Joss and Waldvogel V_t-Z relationship or a Marshall-Palmer type DSD could be overestimating the droplet concentration, underestimating the size of the raindrops, and thus underestimating the terminal fall speeds of the raindrops.

Regions classified as dry snow made use of the V_t-Z relationship derived by Atlas et al. (1973) (Eqn. 2.15):

$$V_t = 0.817Z^{0.063} \qquad [\text{m s}^{-1}] \qquad (2.15)$$

where Z is in units of mm^6 m^{-3}.

Terminal velocity computation for graupel assumed an exponential size distribution (Eqn. 2.16):

$$N(D) = N_o e^{-\lambda D} \qquad [\text{m}^{-4}] \qquad (2.16)$$

where N_o is the slope intercept in units of m^{-4}, D is the diameter in m, and Λ is the slope of the distribution in m^{-1} (Doviak and Zrnić 1993). N_o was an assumed 40,000 m^{-4} (Lin 1983) while values of Λ were backed out directly from the reflectivity measurements. The radar-derived mass-weighted terminal fall velocity of an ice particle (graupel, hail) is equal to the quotient of the precipitation rate (R) over the particle ice water content (IWC) (Eqn. 2.17).

$$V_t = \frac{R}{IWC} \qquad [\text{m s}^{-1}] \qquad (2.17)$$

$$R = \int_0^\infty \frac{\pi}{6} \rho N_o D^3 e^{-\lambda D} v(D) dD \qquad [\text{kg m}^{-2}\ \text{s}^{-1}] \qquad (2.18)$$

$$IWC = \int_0^\infty \frac{\pi}{6} \rho N_o D^3 e^{-\lambda D} dD \qquad [\text{kg m}^{-3}] \qquad (2.19)$$

ρ is the particle density in units of kg m^{-3} (assumed constant), N_o is the slope intercept in m^{-4}, Λ is the slope of the distribution in m^{-1}, D is the particle diameter in m, and v(D) is the terminal fall speed of a particle with diameter D in m s^{-1} (Doviak and Zrnić 1993). A power law-based relationship was assumed for v(D), taken from Locatelli and Hobbes (1974) (Eqn. 2.20):

$$v(D) = 1.3 D^{0.66} \qquad [\text{m s}^{-1}] \qquad (2.20)$$

D is in units of mm. The terminal velocities of hail were estimated in the same way as graupel. However, N_o was assumed to be 10,000 m^{-4} (Ulbrich 1977), and the equation for v(D) was taken from Ulbrich (1977) (Eqn. 2.21):

$$v(D) = 16.2 D^{0.5} \qquad [\text{m s}^{-1}] \qquad (2.21)$$

D is in units of mm. In regions classified as rain-hail mixtures, the terminal velocities were estimated by taking the mean of the hail and rain V_t calculations. All hydrometeor fall speed calculations were adjusted for air density following Beard (1985).

V_t estimations in wet snow (the melting layer) were based on various interpolation methods and dependent upon a profile's precipitation regime (section 2.2.3). If a profile was labeled as convective or mixed stratiform/convective, a linear interpolation scheme was utilized where the water to ice ratio was assumed to equal one at the top of the melting layer and zero at the base. In stratiform regions, multiple interpolation techniques were introduced, including those where V_t varied exponentially, linearly, and by different power laws, where V_t gradually increased to some maximum value before decreasing back to a boundary value, and where V_t followed the finite difference Doppler velocity gradient (V_t based on V_d at range gate+1 and range gate-1). The V_t interpolation method of choice was that which created a V_t profile whose vertical gradient followed best with the actual vertical Doppler velocity gradient in the melting layer (ΔV_d from two successive range gates).

2.3 Vertical Air Motion Verification Techniques

2.3.1 EVAD

Lhermitte and Atlas (1961) first described in detail how horizontal wind measurements by a single Doppler radar can be used in regions of wide spread echo coverage to determine the wind speed and direction, as well as particle fall speed (vertical air motion + particle terminal fall velocity). They proposed a scanning strategy in which the radar beam is directed at constant elevation angle. As the beam rotates, the radar

provides an output of the radial velocity of precipitation particles versus azimuth, or a velocity-azimuth display (VAD). Caton (1963) and Browning and Wexler (1968) extended the VAD concept to the retrieval of divergence in the wind field. When creating a VAD, the horizontal wind field is approximated as a first order Taylor series. The VAD scanning strategy performed at multiple elevation angles can lead to the creation of mean profiles of horizontal winds, particle fall speed, vertical velocity (using particle terminal fall velocity assumptions), and divergence. The concept of EVAD (extended velocity-azimuth display) was proposed by Srivastava et al. (1986). This method is similar to VAD but extends to higher elevation angles and allows for higher variations in the wind field, because the horizontal winds in EVAD are approximated as a quadratic expansion of the Taylor series. For a complete description of the EVAD method, see Srivastava et al. (1986) and Matejka and Srivastava (1991).

Numerous studies have used EVAD to examine the mesoscale structure in both tropical and mid-latitude MCSs (Rutledge et al. 1988; Keenan and Rutledge 1993; Cifelli et al. 1996; etc.). This study utilized S-Pol EVAD analyses from NAME to estimate vertical air motions in stratiform rainfall and compared them with the S-band profiler vertical air motion retrievals.

2.3.2 449-MHz Profiler Results

Profilers observe and record the Doppler velocity spectra at each range gate. When calibrated to the Rayleigh scattering from liquid raindrops, the Doppler velocity spectra can be expressed in reflectivity spectral density units ($mm^6\ m^{-3}$ / $m\ s^{-1}$). The total reflectivity is determined by integrating the reflectivity spectral density over the valid

velocity range (Williams et al. 2006). The observed 449-MHz Doppler velocity reflectivity spectral density for a single profile of precipitation will result in two spectral peaks, one associated with the raindrops within the radar pulse volume and the other with the ambient air motion. An example of a Doppler velocity reflectivity spectral density plot at 449 MHz is shown in Figure 2.12. For more information on 449 MHz vertical air motion retrievals, see Williams et al. (2006).

2.4 Precipitation Frequency Distribution Profiles

A goal of this project was to examine the vertical structure of precipitation events that passed over the profiler site during NAME. Therefore, the S-band dataset was represented in a bulk frequency distribution format as a function of height. This set-up provided no information on the temporal variability or persistence of individual profiles, but provided statistical mean profiles of various radar-derived parameters for different precipitation regimes during NAME. The resulting statistical characteristics of the dataset in this format could then be compared with scanning radar data presented as "contoured frequency by altitude diagrams" (CFADs) (Yuter and Houze 1993, 1995; Steiner et al. 1995) as well as datasets presented as mean profiles (such as EVADs).

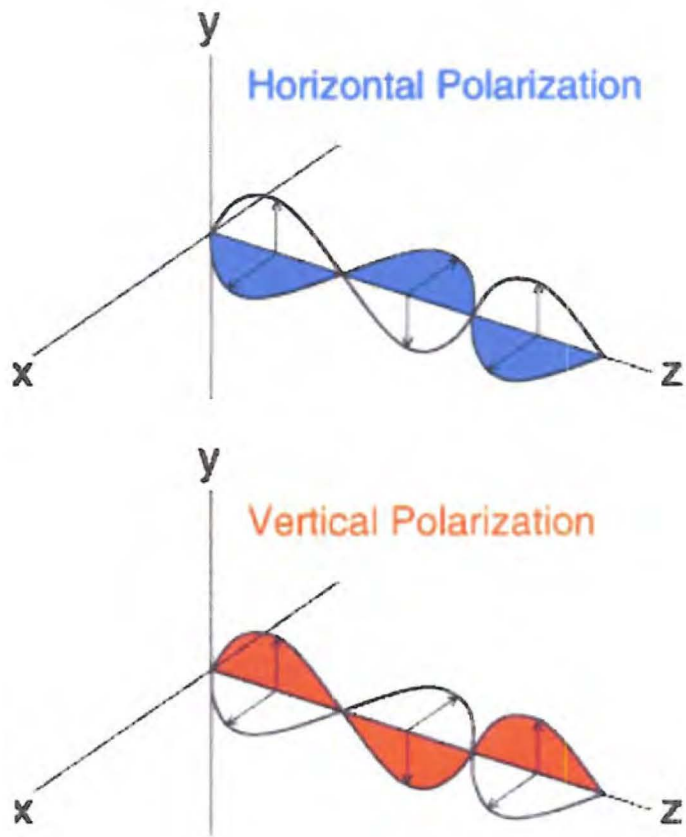

Figure 2.1: Illustration of a horizontally- (top) and vertically- (bottom) polarized electromagnetic wave.

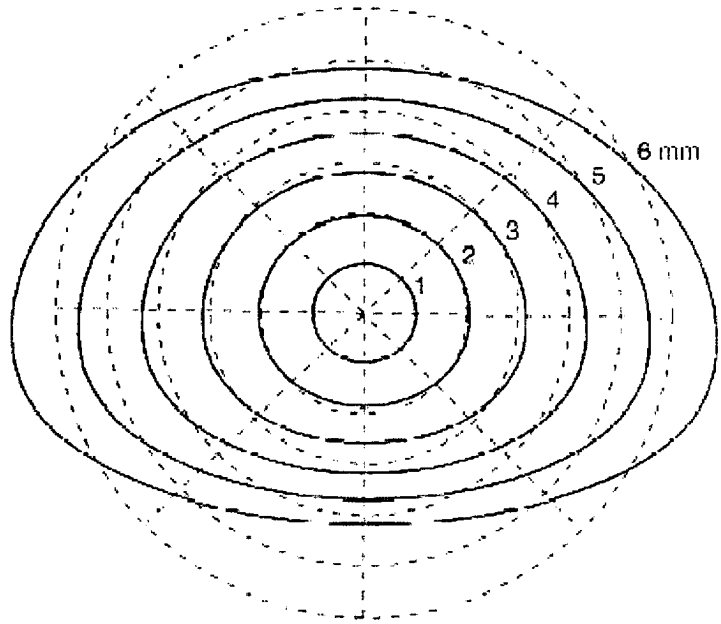

Figure 2.2: Equilibrium drop shapes for drop diameters of 1 – 6 mm (from Beard and Chuang 1987).

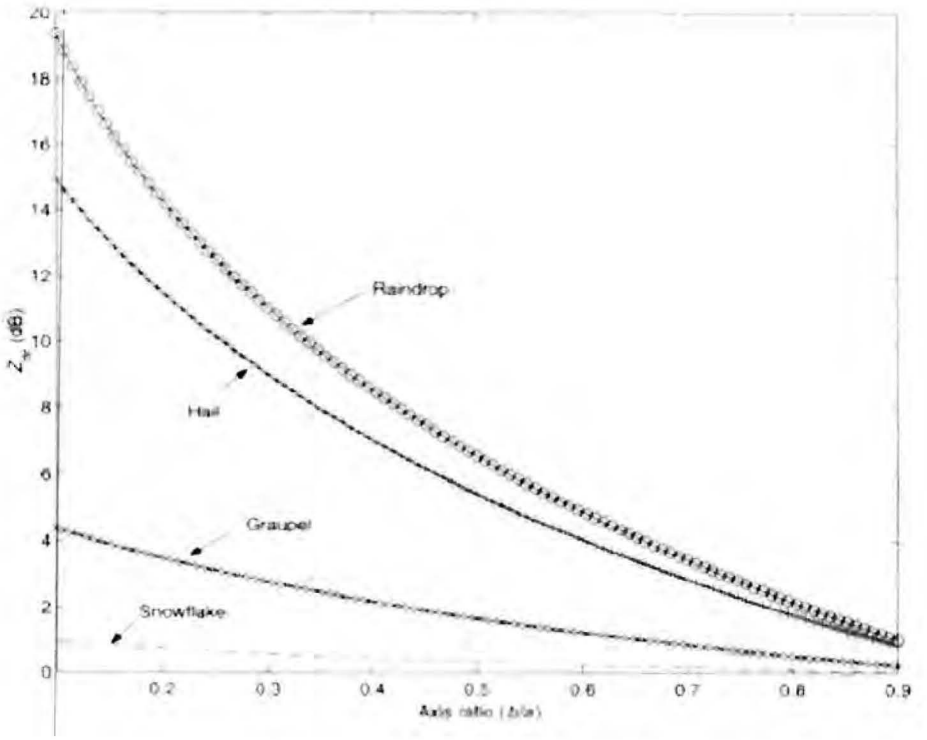

Figure 2.3: Axis ratio, b/a, versus differential reflectivity, Z_{dr}, for various particle types (densities) (from Bringi and Chandrasekar 2001).

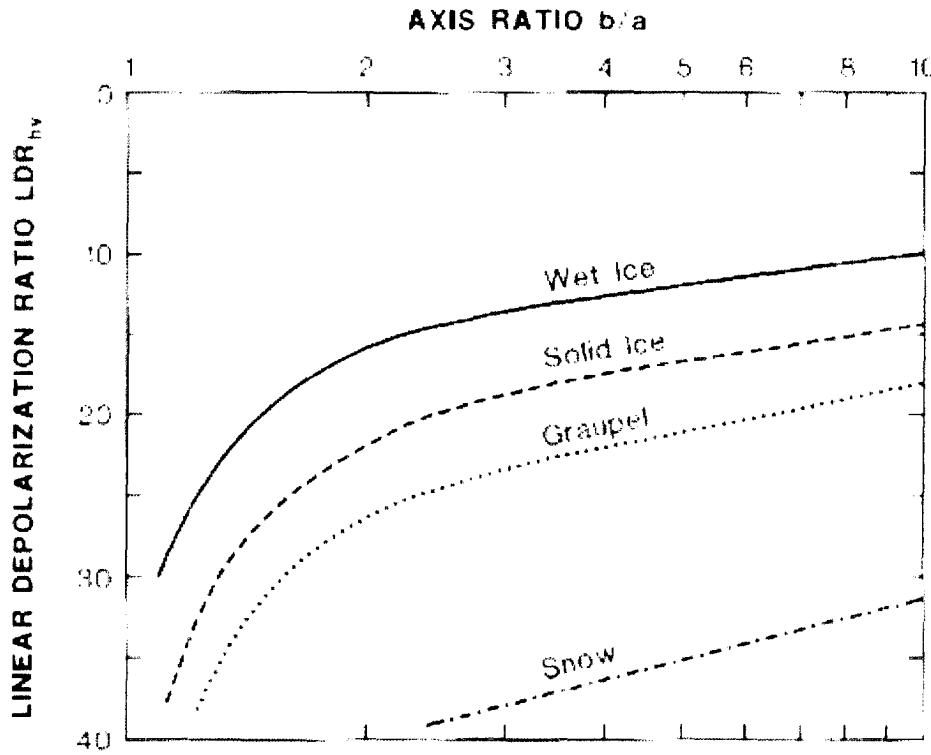

Figure 2.4: Linear depolarization ratio, LDR, as a function of axis ratio, b/a, for various tumbling ice particles (from Doviak and Zrnić 1993).

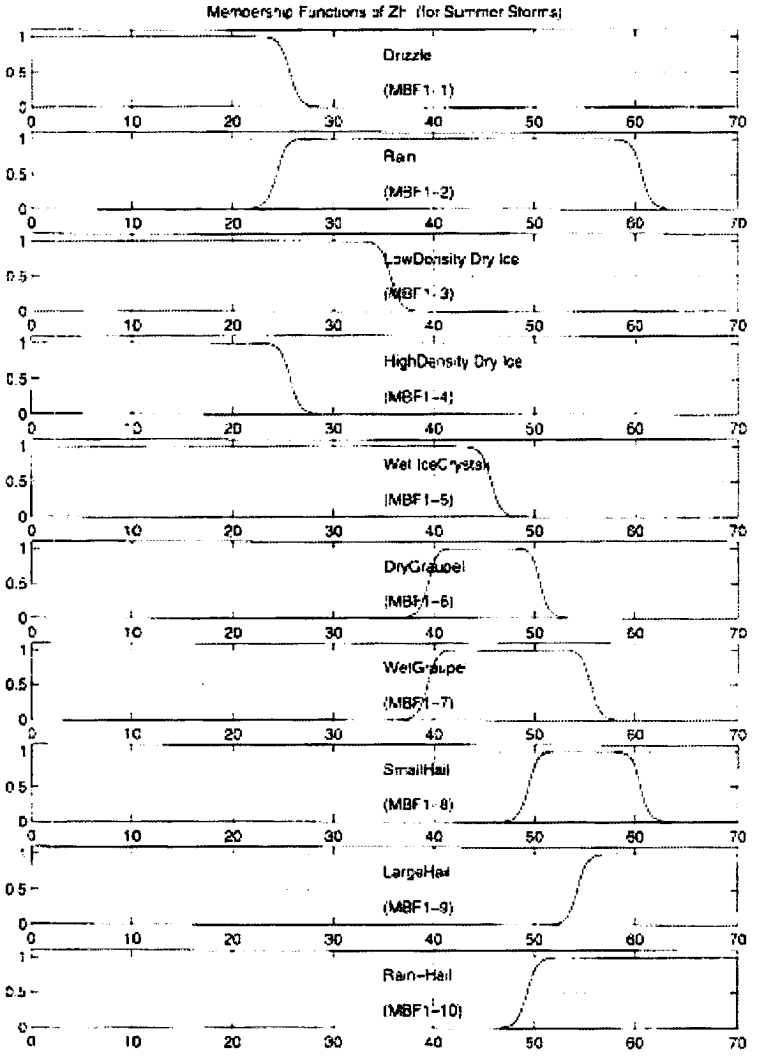

Figure 2.5: Membership functions for fuzzy variable Z_h, and illustration of the fuzzification of Z_h to its 10 fuzzy sets (from Liu and Chandrasekar 2000).

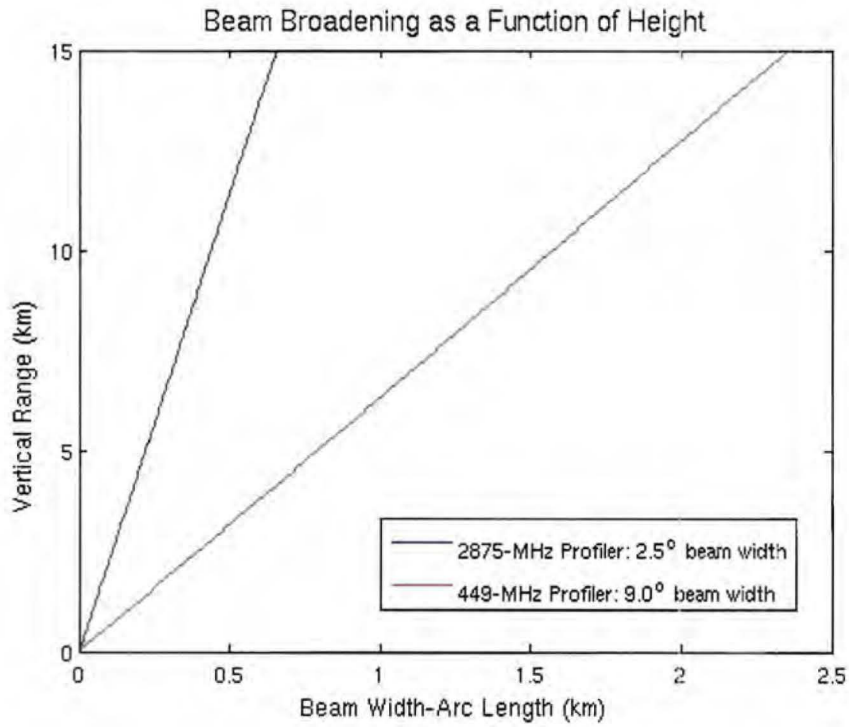

Figure 2.6: 2875-MHz profiler (blue) and 449-MHz profiler (red) beam width broadening with range. Actual curves plotted are $r \cdot \Theta$ (arc length), where r is the range in km and Θ is the profiler beam width in radians. The 2875-MHz profiler beam width is 2.5°, and the 449-MHz profiler beam width is 9.0°.

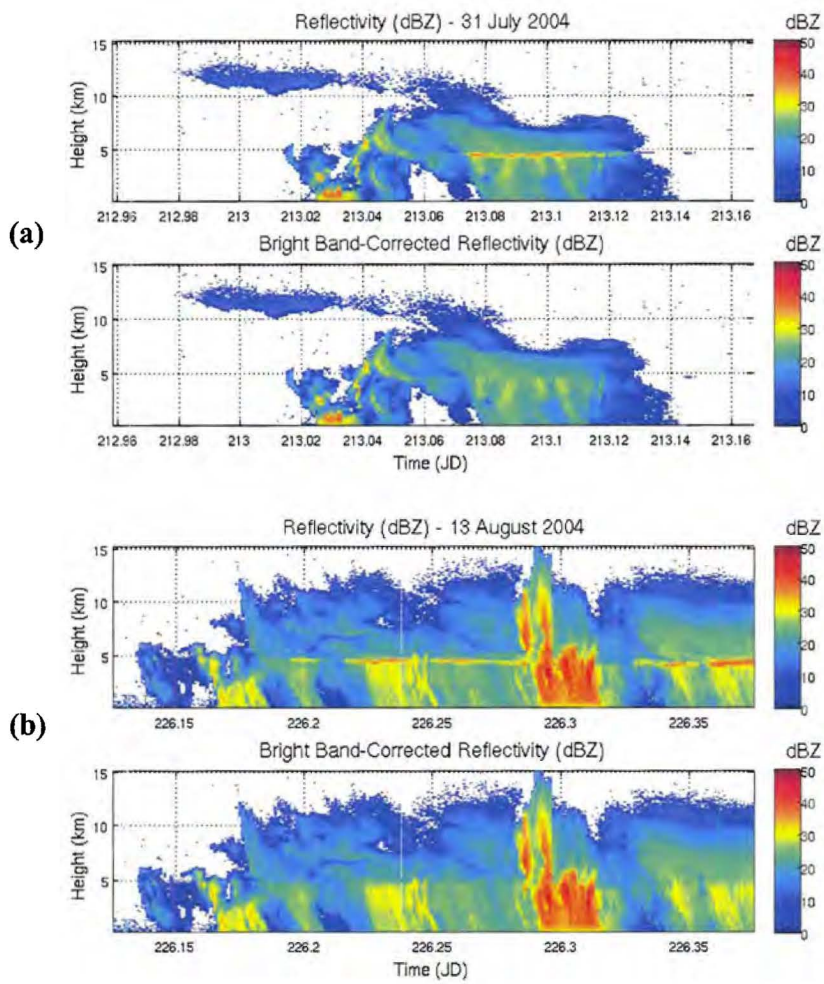

Figure 2.7: Time vs. height contour plots of raw and corrected-reflectivity for the (a) 31 July 2004 and (b) 13 August 2004 NAME S-band profiler events. The upper and lower panels display raw reflectivity and bright band-corrected reflectivity, respectively.

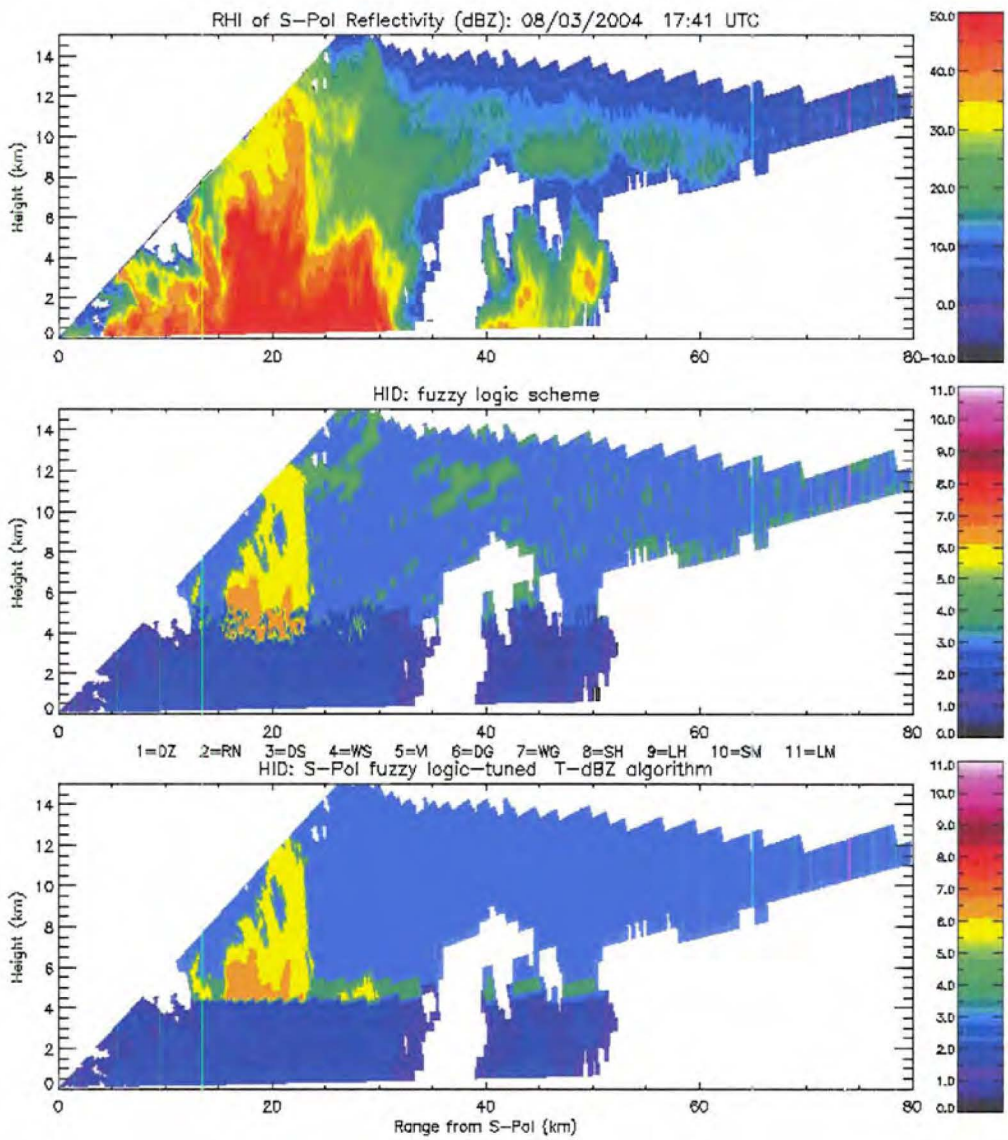

Figure 2.8: RHIs of (a) S-Pol reflectivity, (b) fuzzy logic HID, and (c) HID using the simplified look-up table based on reflectivity and temperature. The RHI was taken at an azimuth of 331° on 3 August 2004 at 17:41 UTC. An HID value of one (violet) corresponds to drizzle. Two (dark blue) is rain, three (light blue) is dry snow, four (dark green) is wet snow, five (bright green) is vertically aligned ice, six (yellow) is dry graupel, and seven (orange) is wet graupel. The other four HID types are not present in this example. Note that the simplified algorithm does not distinguish vertical ice from dry snow, because this requires knowledge of the polarimetric radar variables. Any contours in the lower image suggesting otherwise are purely contouring effects.

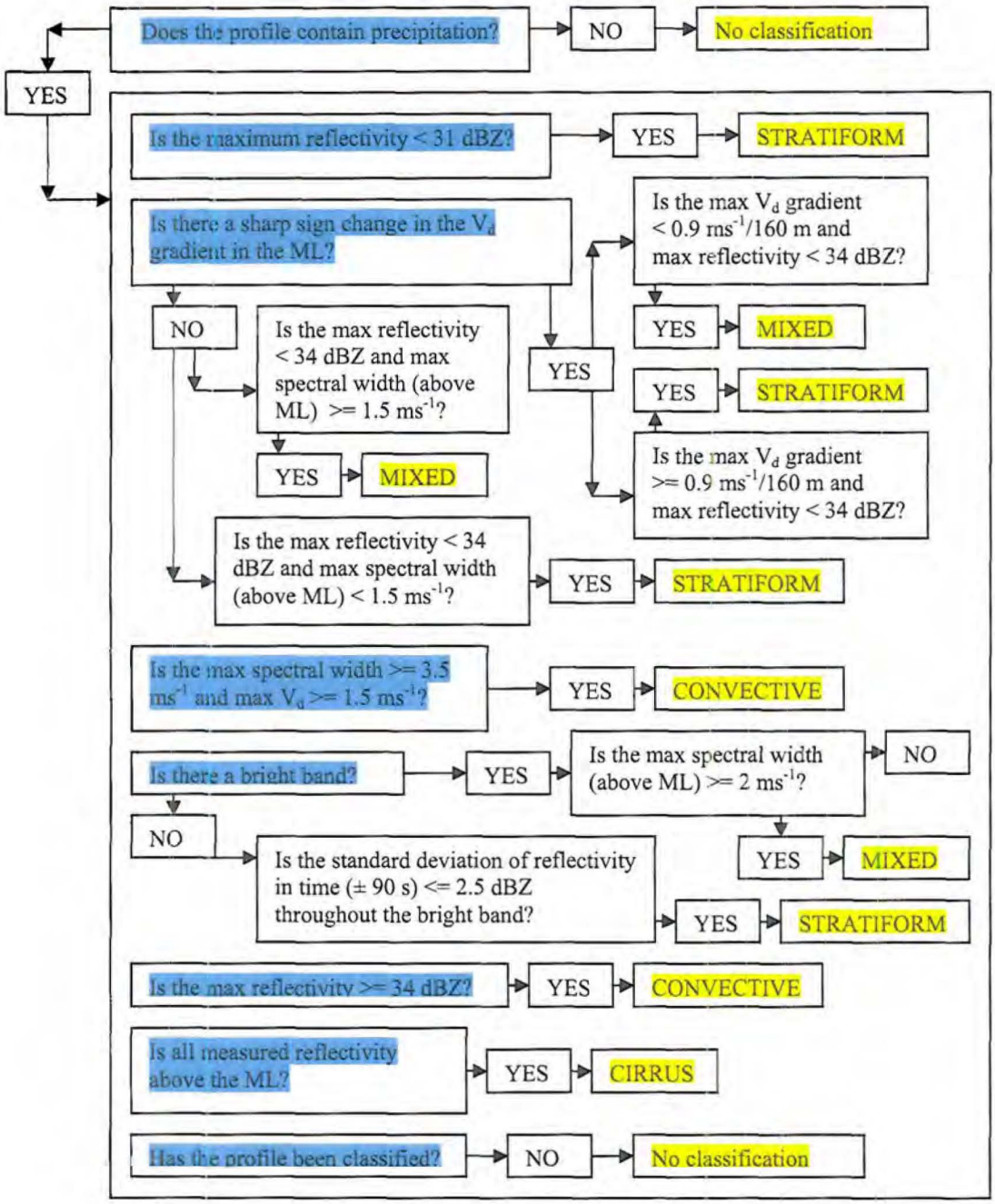

Figure 2.9: The precipitation regime classification algorithm created for this study. The algorithm consists of a string of "if" statements that eventually place a profile of precipitation into one of five categories: 0) stratiform 1) convective 2) mixed stratiform/convective 3) cirrus 4) unclassifiable.

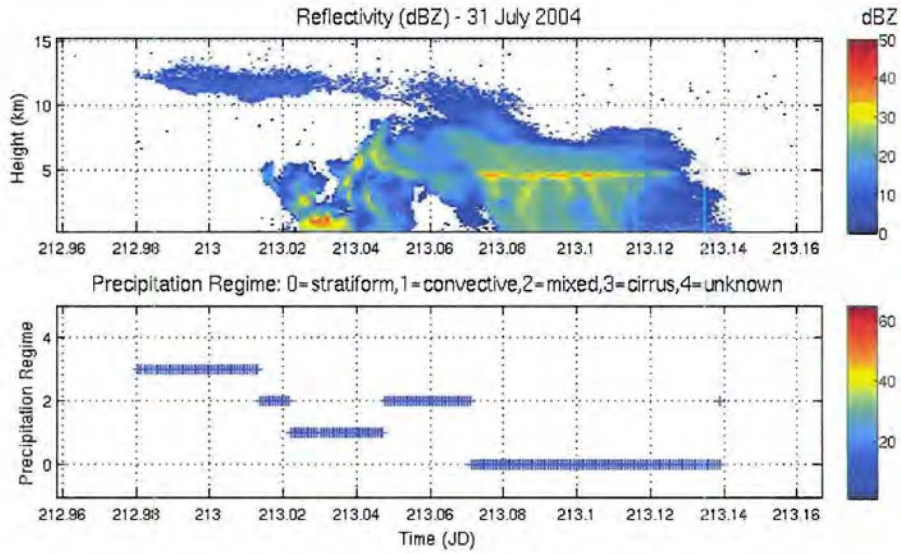

Figure 2.10: Precipitation regime classification for the 31 July 2004 rain event. The top panel shows reflectivity and the lower panel shows the precipitation regime classified with each profile.

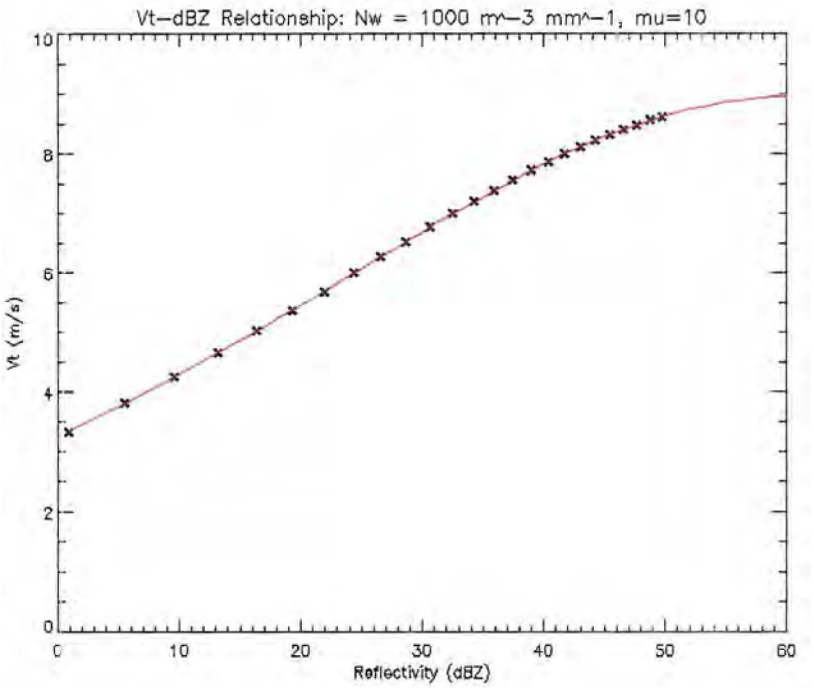

Figure 2.11: The V_t-Z relationship used in this study based on a N_w of 1000 m^{-1} m^{-3} and μ of 10. The data points ('x') are V_t-Z pairs as a function of D_o. The curve is a sixth order polynomial fitted to the data.

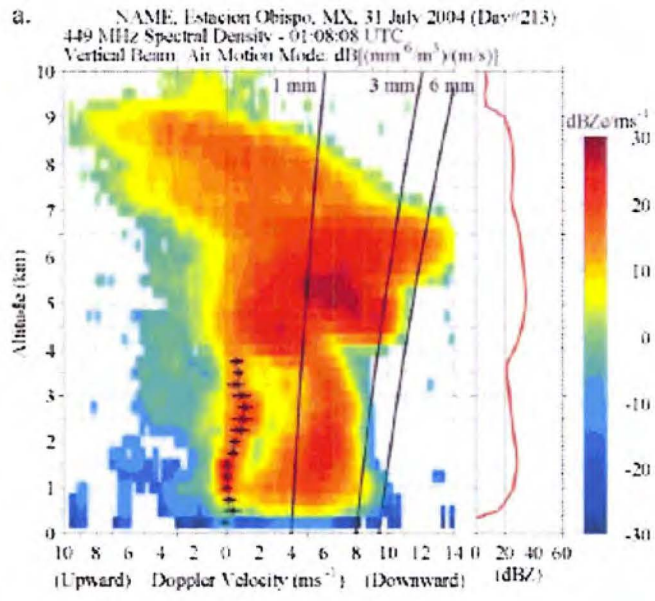

Figure 2.12: Reflectivity Doppler velocity spectral density observed on 31 July 2004 by the 449-MHz profiler at 01:08:08 UTC. The lines labeled '1 mm', '3 mm', and '6 mm' represent the air density corrected terminal velocities for spherical drops having these diameters. The vertical profile of high spectral density near 0 m s^{-1} in the lowest 4 km is associated with the ambient vertical air motion (from Williams et al. 2006).

Species	Z_H (dBZ)	Z_{DR} (dB)	$\rho_{HV}(0)$	K_{DP} (° km^{-1})	Temperature (°C)
Drizzle	10–25	0.2–0.7	>0.97	0–0.06	>−10
Rain	25–60	0.5–4	>0.95	0–20	>−10
Snow (dry, low density; DLD)	−10 to 35	−0.5 to 0.5	>0.95	−1 to 1	<0
Snow* (dry, high density; DHD)	−10 to 35	0.0–1	>0.95	0–0.4	<0
Snow (wet, melting)	20–45	0.5–3	0.5–0.9	0–1	0–5
Graupel, dry (D)	20–35	−0.5 to 1	>0.95	0–1	<0
Graupel, wet (W)	30–50	−0.5 to 2	>0.95	0–3	−15 to 20
Hail, small <2 cm wet (SW)	50–60	−0.5 to 0.5	0.92–0.95	−1 to 1	−15 to 20
Hail, large >2 cm wet (LW)	55–65	−1 to 0.5	0.90–0.92	−1 to 2	−15 to 20
Rain and hail (R/H)	45–80	−1 to 6	>0.9	0–20	−10 to 25

* Rimed and aggregated snow.

Table 2.1: Ranges of polarimetric variables and temperature for various hydrometeor species (from May and Keenan 2005).

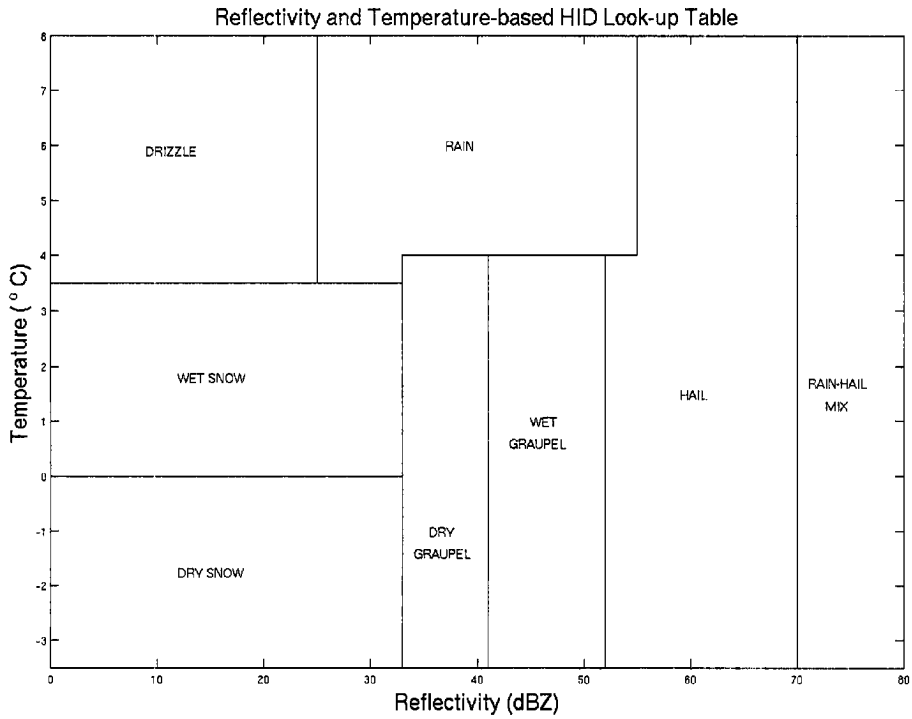

Table 2.2: Look-up table for NAME hydrometeor identification based on S-band reflectivity and temperature.

D_o (mm)	V_t (m/s)
0.4	2.25
0.5	2.8
0.6	3.33
0.7	3.81
0.8	4.25
0.9	4.66
1	5.03
1.1	5.37
1.2	5.69
1.3	5.99
1.4	6.27
1.5	6.53
1.6	6.77
1.7	6.99
1.8	7.2
1.9	7.39
2	7.56
2.1	7.72
2.2	7.86
2.3	7.99
2.4	8.11
2.5	8.22
2.6	8.32
2.7	8.41
2.8	8.49
2.9	8.56
3	8.62

Table 2.3: Terminal fall velocities of raindrops for various values of D_o (Beard 1976).

CHAPTER 3

Results

3.1 Example Case 1: 30-31 July 2004

The 30-31 July precipitation event was characteristic of the NAM regional diurnal cycle with an onset of afternoon surface heating and topographic forcing that led to organized and self-sustained evening convection. Figure 3.1 shows four infrared GOES satellite images of the event. Sporadic convective cells developed over the Sierra Madre near 2015 UTC (a), began to merge and organize along the coast around 2315 UTC (b), and formed three distinct cells by 0145 UTC (c). The central cell continued to strengthen into a mature MCS as it moved up the Mexican coast near 0345 UTC (d). Figure 3.2 depicts the precipitation event over the NOAA profiler site as observed by the S-Pol radar at 1.3° elevation angle. The PPI images depict rain processes and are void of frozen hydrometeors, as inferred from corresponding plots of fuzzy HID (not shown). The cell traveled northeasterly with only its southern tip passing directly over the profiler site, dropping 1.3 mm of rainfall. After the cell's passing, convection dissipated and was followed only by light stratiform precipitation and 0.5 mm of rain. Figure 3.3 shows the vertical structure of the precipitation with time as it passed over the 2875-MHz profiler. The event began with the passage of anvil clouds around 2330 UTC from upper level storm outflow. The convective cell moved over the profiler from approximately 0030 UTC through 0130 UTC, exhibiting both an updraft and downdraft presence. This cell

had updrafts of 4 m s^{-1} near 3 km that preceded the occurrence of large reflectivity at this same altitude. The increased reflectivity was due to larger drops falling out of the updraft while the smaller raindrops were lifted in the updraft (Atlas and Williams 2003; Atlas et al. 2004). Peak updrafts in this cell reached 8 m s^{-1} while downdrafts achieved 7 m s^{-1}. Upward vertical air motions were accompanied by high values of spectral width (> 4 m s^{-1}), indicating that the updrafts contained the most turbulent motions in the system. As the system passed, regions of strong positive vertical air motion progressed in time from heights near the surface to 8 km, suggesting a tilted updraft. While downward air motions remained at mid levels, a low-level downdraft was evident between 0120 and 0140 UTC that lowered in altitude with time. To examine the cell's vertical structure with range, multiple RHI scans were made with S-Pol through the convective cell (331° azimuth) as it passed over the profiler site. The RHI scan taken at 00:52:24 UTC is depicted in Figure 3.4. It is clear that the main convection was north of the profiler site (greater range) while a smaller convective cell was located just to the south (lesser range). Low-level inflow winds converged with the system at a range of 50 km from S-Pol, seen as the transition from flow away from the radar at 5 m s^{-1} (yellow) to flow toward the radar at 15 m s^{-1} (light blue). Storm-top divergence occurred at a range near 60 km. The precipitation over the profiler site transitioned from convective rainfall to mixed stratiform/convective rainfall at approximately 0130 UTC (Figure 3.3). This region was characterized by low reflectivity, upper level regions of ascent with associated high values of spectral width, mid-level downdrafts on the order of 3 m s^{-1}, and stagnant air motion (~ 0 m s^{-1}) at lower levels with slight positive vertical motions of nearly 1 m s^{-1} just below the melting layer. Once the precipitation regime over the profiler

became stratiform at 0140 UTC, three features in the melting layer became apparent. A bright band was clearly visible in the reflectivity profiles. The vertical Doppler velocity gradient sharpened significantly from values near -2 m s^{-1} just above the freezing level to values less than –8 m s^{-1} just below it. This intensification was due to the transition from snow and ice particles falling at 1 to 2 m s^{-1} above the freezing level to raindrops falling at 6 to 8 m s^{-1} below it. This also led to rather high spectral widths (3 to 4 m s^{-1}) near the freezing level while values just above the melting layer dropped below 1 m s^{-1}, suggesting the lack of turbulent air motions just above the melting layer.

3.2 Example Case 2: 13 August 2004

The 13 August 2004 rainfall event over the profiler site was characterized by a nocturnal MCS that produced widespread stratiform precipitation with multiple embedded convective cells. Figure 3.5 shows four infrared GOES satellite images from 13 August 2004. Convection began to organize along the southwest Mexican coast near 0145 UTC (a). By 0345 UTC, organization had led to multiple MCS formation (b). The northern MCS passed over the profiler site just after 0645 UTC (c). As the two systems weakened, they continued to wrap anticyclonically around one another as new convection formed at their boundary (d). Figure 3.6 displays S-Pol reflectivity and mean Doppler velocity as the precipitation moved over the profiler site. Developing convection approached from the southeast. The southwestern portion of a line of convective cells reached the profiler near 0347 UTC (top panels), and new convection formed north of S-Pol around 0547 UTC (middle panels). From approximately 0700 to 0730 UTC, a mature convective cell passed over the profiler site (lower panels) and dropped 25.9 mm

of rainfall. The cell's passing was followed by widespread stratiform precipitation throughout the morning hours (not shown). The on-site rain gauge recorded 9.4 mm of stratiform rainfall between 0300 and 0900 UTC. Figure 3.7 shows the vertical structure of the precipitation with time over the NOAA super site as observed by the 2875-MHz profiler. Low-level precipitation classified as mixed stratiform/convective first reached the site around 0315 UTC, accompanied by modest reflectivity (< 25 dBZ), moderate spectral width below the melting layer (2 to 4 m s^{-1}), and positive vertical air motions on the order of 2 m s^{-1}. By 0350 UTC, this progressed into stronger shallow convection, with reflectivity greater than 35 dBZ in the lowest 5 km. This convection contained regions of moderate turbulence (high spectral width) and positive vertical air motions of 5 m s^{-1}. This passing cell was part of a larger system characterized by multiple cells embedded in stratiform rain (Figure 3.6a). Around 0415 UTC, an upper-level downdraft was detected with a maximum intensity of 9 m s^{-1}. This downdraft lasted 15 minutes and was immediately followed by a brief updraft presence of 5 m s^{-1} at 10 km. Meanwhile, vertical air motions in the lowest 5 km were relatively weak with slight positive motions just below the freezing level. The next 1.5 hours were characterized primarily by stratiform precipitation with a short convective element passing near 0550 UTC. As in the 30-31 July case, the stratiform precipitation was characterized by a reflectivity bright band, strong Doppler velocity gradients, and low spectral width values just above the freezing level. These profiles showed positive vertical air motions around 1 to 2 m s^{-1} above 8 km. However, associated values of spectral width were negligible. There was a reduction in the radar bright band just after 0630 UTC, which may have been due to enhanced subsidence in the region. A 15 km wide convective cell passed directly over

the profiler site from 0645 UTC to 0730 UTC (Figure 3.6e), containing strong updrafts and downdrafts. The vertical air motion profiles revealed alternating fingers of upward and downward vertical air motions at upper levels throughout the cell's passing, suggesting the profiler may have been situated under an updraft-downdraft boundary. At 0650 UTC, the profiler scanned an upper level region (5 to 11 km) of reflectivity greater than 40 dBZ associated with graupel falling at 4 m s^{-1}. This region contained a mixture of both upward vertical air motions less than 3 m s^{-1} and downward vertical air motions as strong as 5 m s^{-1}. Updrafts near 7 m s^{-1} existed just above this region. These profiles were indicative of graupel particles falling through updrafts too weak to support them, possibly after they had been ejected out of the stronger updraft above. Graupel particles were also present in the downdrafts, verified by S-Pol HID analyses (not shown). A similar feature is seen just after 0700 UTC but here the graupel region extended to the base of the melting layer and reflectivity greater than 40 dBZ extended from 10 km down to the surface, indicative of heavy precipitation. This region contained downdrafts on the order of 5 m s^{-1} and was possibly an area where graupel particles moved through the melting layer prior to complete melting. Recall that the simplified HID algorithm used in this study would have been unable to identify any graupel or ice particles that had fallen through the melting layer before completely melting. At 0720 UTC, the profiler scanned another graupel-dominated region between 4 and 5 km. However, this region was associated with a mid-level updraft on the order of 7 m s^{-1}. The graupel was only falling at 3 to 4 m s^{-1} (Figure 3.7e), indicating that the graupel was being lifted in the storm. This means that the downdrafts were both strong enough and cold enough to transport graupel particles below 4 km (i.e. the base of the melting layer), thus allowing them to be

re-circulated upward by low- to mid-level updrafts. Unfortunately, the poor vertical resolution of the S-Pol surveillance scans resulted in measurements over the profiler at heights of 2.5 (3.2° scan) and 4.5 km (5.8° scan) only. While the S-Pol HID analysis identified only rain at 2.5 km during this time (not shown), it is not possible to determine if any ice particles had fallen between 2.5 and 4.5 km with S-Pol. From 0725 to 0735 UTC, the convective cell dropped heavy, continuous precipitation over the profiler site and exhibited downdrafts at all levels between 1 and 5 m s^{-1}. It would have been useful to analyze the convective cell in two-dimensional space between 0650 and 0735 UTC. Unfortunately, no RHI scans were performed with S-Pol over the profiler site during the cell's passage. It is therefore unclear as to what exact microphysical processes were taking place. The convection was followed by a mixed stratiform/convective regime until 0750 UTC, apparent as profiles of low reflectivity with no clear bright band and spectral width near 3 m s^{-1} just above the melting layer. All precipitation that followed was stratiform. The profiler took continuous measurements until approximately 1000 UTC (not shown) when a power outage occurred.

3.3 Verification Results

A primary goal of this study was to estimate vertical air motions from the NAME 2875-MHz profiler dataset. The methodology employed multiple assumptions in estimating the mean particle terminal fall velocity within individual sample volumes, not to mention the error in the measured mean Doppler velocity itself. This certainly led to errors in the vertical air motion retrievals. The retrieved vertical air motions were compared with both EVAD and 449-MHz profiler results for specific cases to assess the

credibility of the 2875-MHz profiler-based retrievals. While the EVAD technique created mean profiles of vertical air motion throughout the layer of precipitation, the 449-MHz profiler provided high spatial and temporal resolution profiles within the lowest 4 km only (below the melting layer). Note that limitations in both techniques allowed only for estimations of vertical air motions within stratiform precipitation.

3.3.1 EVAD

EVAD-derived vertical air motions are not without error. Aside from the uncertainty in the Doppler velocity estimates, errors arise from echo gaps in the radar volume, assumed boundary conditions, and the integration methods used (Srivastava et al. 1986). While the errors are often on the order of the vertical air motion estimates, the EVAD solution provides insight into the general vertical structure of the vertical air motion in a mean sense.

Mean profiles of vertical air motion were successfully derived using the EVAD technique for both the 4 August and 5 August NAME rainfall events. These profiles were representative of the stratiform precipitation throughout the S-Pol domain up to 60 km range. Approximately one hour's worth of individual stratiform profiles of vertical air motion from the 2875-MHz profiler were averaged in time (for each case) for comparison with the EVAD technique. One-hour profiler averages were chosen to represent the EVAD domains based on mean storm advection speeds. Examples from the 4 August and 5 August events are illustrated in Figure 3.8. Profiles of vertical air motion from both the EVAD solution (black) and the 2875-MHz profiler (blue) are displayed in the upper panels. The lower panels show PPI images of reflectivity at 3.2° elevation

angle depicting the precipitation coverage over the S-Pol domain utilized in the EVAD technique. The left hand panels are plots of the 4 August case at 0545 UTC while the right hand panels are of the 5 August case at 2330 UTC. In both cases, the profiler-based vertical air motion compared reasonably well with that of the EVAD solution, showing similar trends and magnitudes. However, the profiler estimates contained a negative bias to the EVAD profiles by as much as 0.6 m s^{-1}. Given the very different nature of these techniques, better agreement cannot be expected.

3.3.2 449-MHz Profiler

The vertical air motions derived from the 449-MHz profiler spectral densities were subject to errors in the measured Doppler velocity and reflectivity fields. The resulting errors in the air motion estimates themselves were as high as 0.5 m s^{-1} (Williams et al. 2006). Since the errors in the derived vertical air motions for both the 449-MHz and 2875-MHz profilers were of the same magnitude as the actual vertical air motions, the results were compared in a bulk sense.

Vertical air motions were derived from the 449-MHz profiler for 13 August 2004 dataset. Frequency distributions of vertical air motion for both profilers are depicted in Figure 3.9. The 449-MHz profiler plot shows a concentration in occurrences near 0 m s^{-1} ($\pm$ 0.5 m s^{-1}) in the lowest 4 km. The main concentrations in frequency for the 2875-MHz profiler appear to be near –0.4 m s^{-1} ($\pm$ 1 m s^{-1}). The distributions of vertical air motion are significantly broader in the 2875-MHz profiler case, indicating that larger uncertainties exist with these estimations. These uncertainties are most likely due to the reflectivity dependence in the 2875-MHz profiler estimations. Similar to the EVAD

comparison, the 449-MHz profiler results indicate that the 2875-MHz profiler air motions have a mean negative bias of almost 0.5 m s^{-1}.

3.4 Precipitation Frequency Distribution Profiles for NAME

The NOAA 2875-MHz profiler recorded 6008 profiles of precipitation during 23 NAME rain events. These profiles were associated with 142.5 mm of rainfall as measured by the onsite tipping bucket rain gauge. Of the 6008 profiles, 3671 were classified as stratiform (61.1 %), 749 as convective (12.5 %), and 1588 as mixed stratiform/convective (26.4 %). However, of the 142.5 mm of rain, 101.3 mm was associated with convective rainfall (71.1 %), 23.9 mm with stratiform rainfall (16.8 %), and 17.3 mm with mixed stratiform/convective rainfall (12.1 %). Based on the number of profiles, the profiler sampled mainly stratiform precipitation during the 23 NAME events. However, the rainfall was dominated by convective precipitation due to the greater convective rainfall rates. Mean rainfall rates were estimated for each precipitation regime using both the onsite rain gauge data as well as S-Pol rainfall estimates. The mean stratiform rainfall rate as calculated from the rain gauge data was 2.5 mm hr^{-1}. The mean convective rainfall rate was 26.0 mm hr^{-1}, and the mean mixed regime rainfall rate was 9.9 mm hr^{-1}. The mean stratiform rainfall rate calculated using S-Pol was 0.7 mm hr^{-1}. The mean convective rainfall rate was 30.0 mm hr^{-1}, and the mean mixed regime rainfall rate was 1.1 mm hr^{-1}. The S-Pol rainfall rates compared well with those from the tipping bucket rain gauge in the stratiform and convective cases. Assuming the rain gauge solutions to be most accurate, S-Pol slightly overestimated convective rainfall rates by 4 mm hr^{-1} and underestimated stratiform rainfall rates by

1.8 mm hr^{-1}. The mixed stratiform/convective results were not as similar. S-Pol underestimated these rainfall rates by 8.8 mm hr^{-1}. This could be due to multiple factors, including the limited temporal resolution of the S-Pol estimates, the height at which the S-Pol estimations were based, and the polarimetric variables (if any) used in the rainfall rate estimations.

Frequency distributions were created for each precipitation regime, as well as for the entire NAME dataset, and they were compared with similar plots for different regions of the world. Plotted variables included reflectivity, mean Doppler velocity, spectral width, and derived vertical air motion. Only profiles associated with precipitation reaching the surface were used in creating the profiles. However, the onsite Joss-Waldvogel disdrometer (Joss and Waldvogel 1967) dataset proved unusable. Instead, the 2875-MHz profiler dataset was threshold on reflectivity less than 0 dBZ, and only profiles with at least 5 bins with reflectivity greater or equal to 0 dBZ in the lowest 2 km were included. Reflectivity was distributed into 1 dBZ-wide bins from 0 to 50 dBZ. Doppler velocity, spectral width, and vertical air motion were distributed into 0.2 m s^{-1} bins. The Doppler velocity frequency distribution was plotted from –10 (downward) to 2 (upward) m s^{-1}. Spectral width was plotted from 0 to 5 m s^{-1}, and vertical air motion was plotted from –10 (downward) to 10 (upward) m s^{-1}.

3.4.1 All Cases

The two-dimensional frequency distributions for the entire NAME dataset are illustrated in Figure 3.10. Reflectivity is shown in Figure 3.10a. The distribution of reflectivity in the lower troposphere ranges from 0 to 40 dBZ, with a concentration near

25 dBZ. A reflectivity frequency increase occurs at 4.5 km in the range of 30 to 40 dBZ. This is a manifestation of the radar bright band. Above the bright band, hydrometeors are primarily ice particles, and the Rayleigh scattering intensity decreases with altitude (Williams et al. 1995). This is visible in Figure 3.10a as a decrease in concentrated reflectivity with height.

The mean Doppler velocity frequency distribution is shown in Figure 3.10b. Note that the concentration of Doppler velocity spectra around 0 m s^{-1} in the lowest 2 km is indicative of ground clutter and other noise that was not quality controlled. This artifact will be ignored during the analysis. There is a distinct narrowing of the Doppler velocity spectrum with height starting at 4 km, or the base of the melting layer. Below this altitude, the Doppler velocity ranges from –10 to –2 m s^{-1} with a concentration between –6 and –7 m s^{-1}. This concentration slightly intensifies with height below the melting layer. The Doppler velocity spectra ranges from –5 to 1 m s^{-1} at 4.8 km, and from –3 to 0 m s^{-1} at 12 km. The Doppler velocity is concentrated near –1.5 m s^{-1} above 4.8 km. Recall that the Doppler velocity measurement from a 2875-MHz profiler is primarily the hydrometeor fall velocity convolved with the atmospheric vertical motion. Therefore, the Doppler velocity spectrum at a given height is largely dependent on the distribution of hydrometeor terminal fall speeds at that height. The narrow distribution above 5 km is due to the fact that hydrometeors at these heights are primarily ice particles. While snow falls near 1 to 2 m s^{-1}, large graupel particles fall at speeds on the order of only 2 to 4 m s^{-1} (Wallace and Hobbs 1977). Raindrops of different sizes vary greater in their terminal fall speeds. The broad Doppler velocity spectra below 4 km results from a distribution of raindrop terminal fall velocities. The transition from the wide to the

narrow distribution occurs within the melting layer, where falling snow and ice melt and form raindrops.

The frequency distribution of spectral width is shown in Figure 3.10c. Above 4.8 km, the spectral width has a concentration of occurrences near 0.5 m s^{-1}. Within the melting layer, from 4.8 to 4 km, the distribution increases to 2.5 m s^{-1}. This increase is associated with the broadening of the drop size distribution as individual hydrometeors experience an increase in density and a decrease in cross-sectional area as they fall through the melting layer (Williams et al. 1995). The distribution gradually decreases to 2 m s^{-1} near the surface. The frequency distribution of spectral width broadens within and below the melting layer. This is associated with the broadening of the Doppler velocity spectra from the transition of ice particles to raindrops. Another source of spectral broadening within the melting layer is the acceleration of individual hydrometeors through the radar resolution volume as they change phase from solid to liquid (Williams et al. 1995). The extra broadening that occurs in the lowest 1 km is a noise residual.

The frequency distribution of vertical air motion is shown in Figure 3.10d. A noise presence is visible near 5 m s^{-1} in the lowest 2 km. A concentration in occurrence occurs at roughly 0 m s^{-1} above the melting level and approximately –0.5 m s^{-1} below it. The region of highest concentration also broadens below the melting level, suggesting that there is higher uncertainty in the terminal fall velocity estimations of raindrops compared to those of snow and ice crystals. There also appears to be a secondary (lower frequency occurrence) trend in the vertical air motion with height where the air motion decreases by roughly 3 m s^{-1} within the melting layer, then gradually increases just above

it. This is most likely due to the hydrometeor fall speed uncertainties in the bright band interpolation scheme utilized in this study.

There is a clear dominance of stratiform precipitation in the frequency distribution diagrams. This is evident by a distinct reflectivity bright band presence, steep vertical gradients in both Doppler velocity and spectral width, and vertical air motion frequency concentrations near 0 m s^{-1} at all heights. These factors also indicate that the melting layer was less than 1 km wide (between 4.1 and 4.8 km). However, there are several other features shown in Figure 3.10 that suggest different physical processes were occurring within the profiles. To assess these features, the NAME profiles were categorized by precipitation regime using the algorithm discussed in section 2.2.3. Frequency distribution profiles for each regime are discussed and compared with similar profiles from different geographic regions in sections 3.4.2-4. Such comparisons are complicated by differences in observational techniques, MCS life cycle stage, and the large variation in spatial scales utilized in these studies (Cifelli and Rutledge 1994). Therefore, the results are shown primarily to place the NAME profiles in the context of similar profiles derived from other tropical and mid-latitude locations and to compare their salient features.

3.4.2 Stratiform

Figure 3.11 depicts the frequency distributions of reflectivity, Doppler velocity, spectral width, and vertical air motion for the precipitating cloud profiles classified as stratiform. A defined radar bright band is evident at 4.5 km in Figure 3.11a. Below 4 km, reflectivity ranges between 0 and 30 dBZ with a concentration near 25 dBZ.

Reflectivity increases to values near 33 dBZ in the bright band. Values decrease back to 25 dBZ immediately above the bright band and then continue to decrease with height. This compares well with stratiform profiles of reflectivity from Manus Island, Papua New Guinea using a 915-MHz profiler (Williams et al. 1995), and both Darwin, Australia (Steiner et al. 1995) and the western Amazon (Cifelli et al. 2004) using scanning Doppler radars. Figure 3.12 displays the CFAD of stratiform reflectivity from Darwin, Australia during February 1988. It revealed a concentration of reflectivity near 25 dBZ with a bright band just below 5 km and values decreasing with height above the melting layer. Figure 3.13 shows both reflectivity frequency distributions and profiles of mean reflectivity from the western Amazon. The CFAD plots from both the westerly and easterly regimes showed broader frequency distributions than NAME with reflectivity reaching 40 dBZ below 4 km. However, the profiles in Figure 3.13c showed mean values near 24 dBZ below the melting layer, a radar bright band just below 5 km with slightly enhanced values near 28 dBZ, and decreasing values of reflectivity with height above the melting layer. This matched well with the NAME distributions. Similar results are seen in Figure 3.14a in the Manus Island frequency distribution profile for stratiform precipitation during May 1992 through February 1993.

The NAME Doppler velocity frequency distribution plotted in Figure 3.11b is rather narrow with a concentration of values centered at -1.5 m s^{-1} above the melting layer. There is a maximum in concentration between 5 and 6 km. Velocities increase through the melting layer to -8 m s^{-1} at 4 km as ice particles melt and form raindrops. Concentrated values slightly decrease to -6.5 m s^{-1} near the surface, perhaps due to evaporation or drop breakup. Mean Doppler velocity values from Manus Island (Figure

3.14b) are similar, for values are centered at –6 m s^{-1} near the surface and –7 m s^{-1} at 4 km. The distribution narrows above the melting layer with concentrated values of about –1 m s^{-1}.

The stratiform frequency distribution of NAME spectral width depicted in Figure 3.11c is narrow above the melting layer and centered around 0.5 m s^{-1}. This indicates that these profiles are not turbulent above the melting layer. Spectral width increases to a central value of 2.25 m s^{-1} within the melting layer due to a broadening of the drop size distribution (and thus the hydrometeor fall velocity distribution) from the melting of frozen hydrometeors. The spectral width falls slightly to a concentrated value of 2 m s^{-1} near the surface. The spectral width profile for Manus Island (Figure 3.14c) is again similar, concentrated at 2.5 m s^{-1} near the surface and values gradually increase to 3 m s^{-1} at 4 km. Along with a narrowing of the spectrum, values of spectral width decrease to 1 m s^{-1} above 5.5 km.

It should be noted that in comparing the Doppler velocity and spectral width vertical gradients in stratiform precipitation for NAME and Manus Island, it appears that the melting layer (region where values change rapidly with height) is significantly thinner in the NAME profile. While the NAME melting layer ranges from 4.1 to 4.8 km, the Manus Island melting layer ranges from 4.3 to 5.8 km. However, this is most likely an artifact of the vertical resolution used in the profiles. The NAME profiles, utilizing the pulse length of the 2875-MHz profiler, have a vertical resolution 60 meters. The pulse length of the 915-MHz profiler in "high-height" mode used at Manus Island was 255 meters (Williams et al. 1995). This lowered resolution prevented the 915-MHz profiler data from resolving the melting layer as well as the 2875-MHz profiler. Therefore, the

melting layer is broader and more smeared out in the Manus Island profiles while subtle changes within small height increments are evident in the NAME profiles.

The frequency distribution of NAME vertical air motion in stratiform precipitation is shown in Figure 3.11d. Concentrated values are centered on 0 m s^{-1} above the melting layer. Below the melting layer, central values reach –0.05 m s^{-1}. In stratiform precipitation, some raindrops evaporate as they fall below cloud base, resulting in evaporation and thus a slight cooling of the air in the lower troposphere. This cooling can lead to subsidence. This effect is evident in the vertical air motion profile. However, vertical air motion, based on continuity assumptions, should approach 0 m s^{-1} near the surface. The NAME profile still shows downward motions near the surface. It is likely that the normalized drop size distribution derived for this study from the 13 August case (section 2.2.4) was not universal and resulted in minor underestimations of the raindrop terminal fall speeds. Recall that the vertical air motion is the sum of the Doppler velocity and hydrometeor terminal fall speed (Eqn. 2.10). If the raindrop terminal velocity is underestimated, the result is an underestimation in the vertical air motion.

Cifelli and Rutledge (1994) compared derived vertical air motions in stratiform rainfall for various geographic locations. Figure 3.15 shows the vertical air motion composite for NAME with composites from Darwin, Australia using a 50-MHz profiler (Cifelli and Rutledge 1994), the western Pacific (Pohnpei Island) using composite wind profiler data (Balsley et al. 1988), the South China Sea using composite ship rawinsonde data (Johnson 1982), a West Africa continental tropical MCS using the single-Doppler radar (VAD) retrieval (Chong et al. 1987), a tropical oceanic system in the east Atlantic using rawinsonde and aircraft data (Houze and Rappaport 1984), and a mid-latitude MCS

using the single-Doppler radar (EVAD) retrieval technique (Rutledge et al. 1988). The profiles all indicate descent in the lower troposphere and ascent in the upper troposphere. These regions are present in the NAME profiler-generated composite. The magnitude of both the mesoscale downdraft and updraft is strongest in the NAME and mid-latitude cases. It should be noted that values in the NAME profile decrease to 0.2 m s^{-1} at upper levels while profiles from previous studies approach 0 m s^{-1}. The western Amazon vertical air motion results in Figure 3.16 show distributions ranging from –8 to 8 m s^{-1}. The profile of mean vertical air motion shows values between –0.5 and 0 m s^{-1} near the ground, slightly enhanced subsidence near 5 km, and ascent above 8 km.

3.4.3 Mixed Stratiform / Convective

The frequency distributions for those profiles classified as mixed stratiform/convective are displayed in Figure 3.17. The reflectivity in Figure 3.17a ranges mainly from 0 to 35 dBZ below the melting layer, but there are faint signatures of values greater than 40 dBZ. There is a trace of a radar bright band at 4.5 km. However, this trace is significantly weaker than in the stratiform profiles. The core of reflectivity gradually increases with height from 10 dBZ near the ground to 18 dBZ at 8 km. Concentrated values of reflectivity decrease with height above the melting layer. However, there is a noticeably broader frequency distribution compared to the stratiform profiles. Reflectivity spans from 0 to 30 dBZ in the mixed case. The Manus Island reflectivity spectrum for mixed stratiform/convective precipitation is displayed in Figure 3.18a. The Manus Island spectra reach higher values of reflectivity than NAME in the lowest 4 km. Values range from 15 to 40 dBZ. Above 4 km, the two profiles compare

rather well. Both exhibit a weak bright band presence and decreasing values with height above the melting layer.

The Doppler velocity spectra for mixed precipitation illustrated in Figure 3.17b also varies slightly from the stratiform profiles. The broad distribution in the lowest 4 km is centered at approximately –5 m s^{-1}. The Doppler velocities above the freezing level are between –1 and –2 m s^{-1}. However, the distribution remains broad, ranging from –10 to 2 m s^{-1} between 6 and 12 km. This suggests the presence of downdrafts at upper levels. The Doppler velocity distributions from Manus Island (Figure 3.18b) compare favorably with those from NAME, displaying frequency concentrations near –5 to –6 m s^{-1} at low levels and values near –1 m s^{-1} above the melting layer.

The spectral width frequency distribution for mixed precipitation is plotted in Figure 3.15c. The bulk of the broad distribution below the melting layer ranges from 1 to 2.5 m s^{-1} with a concentration of occurrences near 1.7 m s^{-1}. There is significant concentration around 0.7 m s^{-1} between 5 and 6 km. The central value decreases slightly to 0.5 m s^{-1} above 6 km. However, the distribution remains broad, as is expected for mixed stratiform/convective precipitation. Spectral width varies between 0 and 3.7 m s^{-1} from 4 to 7 km and reaches values to 4 m s^{-1} above 7 km. The frequency distribution does not narrow until a height of 11 km. This indicates the presence of turbulence above the melting layer associated with upper level updrafts and downdrafts. The Manus Island spectral width distributions (Figure 3.18c) show similar trends with a few distinct differences. The spectrum below the melting layer is narrower and centered on higher values (2 to 3 m s^{-1}). Broad distributions due to turbulent motions exist at all heights

above 5 km, and upper level main frequency concentrations are slightly higher than those in NAME, ranging between 1 and 2 m s^{-1}.

The vertical air motion associated with mixed stratiform/convective precipitating clouds is shown in Figure 3.17d. Ignoring the noise at low levels, the distribution varies from –3 to 7 m s^{-1} with the main concentration ranging from –1 to 1 m s^{-1} and centered on 0 m s^{-1}. This means the low-level vertical air motion was generally weak, but there were updraft and downdraft occurrences in the mixed regime. From 2 to 4 km, the concentration of vertical air motions is about 0.8 m s^{-1}. Within the melting layer, values of –1 m s^{-1} at a height of 5 km are found. By 6 km, the main concentration of vertical air motion is 0 m s^{-1} and remains so through the rest of the profile. Frozen hydrometeors falling through the top of the melting layer begin to melt, coalesce with other particles, and thus increase in size and fall speed. These hydrometeors can create slight negative vertical air motions from the drag forces they impose, and thus, the negative motions at 5 km. However, this shift in vertical air motion in the melting layer may also be influenced by the interpolation assumptions used in estimating hydrometeor terminal fall speeds in the melting layer. Above the melting layer, the distribution remains as broad as the distribution below it. However, the range of values shifts to a lower spectrum. Vertical air motions range from –9 to 3 m s^{-1} above 6 km, indicating the presence of updrafts and downdrafts at upper levels.

The mixed regime vertical air motion results from NAME were compared with composites from Darwin, Australia using a 50-MHz profiler (Cifelli and Rutledge 1994), mid-latitude MCSs using dual-Doppler radar (Smull and Houze 1987; Biggerstaff and Houze 1993), a West African tropical squall line using dual Doppler radar (Chalon et al.

1988), and a GATE tropical oceanic system using composite rawinsonde data (Houze and Rappaport 1984). These comparisons are shown in Figure 3.19. The NAME profile does not appear to match best with any previous study in particular. While previous studies show subsidence below the melting level, the NAME profile shows ascent. The profiles from Houze and Rappaport (1984), and Smull and Houze (1987) show ascending air motion in the middle to upper troposphere. Other previous studies show descending motion throughout this region. The profile from NAME shows both features, with descent below 8 km and ascent above. The magnitude of ascent is also greatest in the NAME profile. Note that these comparisons may be influenced by the fact that the various partitioning algorithms used to identify mixed precipitation do so with a fair amount of uncertainty.

3.4.4 Convective

Frequency distributions of those profiles classified as convective are displayed in Figure 3.20. The reflectivity ranges between 0 and 45 dBZ below 5 km as is shown in Figure 3.20a. The major concentration of reflectivity varies between 25 and 40 dBZ, indicating significantly heavier rainfall than in the stratiform or mixed cases. Reflectivity generally decreases with height above 5 km. However, while upper level reflectivity decreases to a central value of 5 dBZ, there is a secondary maximum of reflectivity concentration above 10 km of around 25 dBZ. This means that in some cases, an abnormally large concentration of hydrometeors (or large hydrometeors) reached upper levels of the storms. This is indicative of hydrometeors, such as ice and supercooled raindrops, being transported upward in significant updrafts. The NAME convective

profile compares well with those from Darwin, Australia (Figure 3.21), the western Amazon (Figure 3.22), and Manus Island (Figure 3.23a). The profiles show the bulk of the reflectivity to be between 30 and 40 dBZ below 4 km. Values generally decrease with height and reach values between 10 and 20 dBZ by 10 km. However, the Manus Island profile shows low-level core values near 20 dBZ. The Frequency distributions from the western Amazon showed the most intense convection with the distribution of reflectivity reaching 50 dBZ.

The distribution of Doppler velocity associated with convective precipitation is depicted in Figure 3.20b. In the lowest 2 km, the distribution spans from -3 m s^{-1} to -10 m s^{-1}. This is from both a broad drop size distribution associated with large and small raindrops as well as strong convective downdrafts. The core of the occurrences lay between -5 and -8 m s^{-1}. Above 2 km, the distribution broadens to include Doppler velocities as great as 2 m s^{-1}. However, the region of most noticeable frequency occurrences ($\log_{10}$(frequency) > 1.2) narrows with height to a central value of -7.5 m s^{-1} at 4 km. The melting layer is noticeable, with core values of Doppler velocity gradually increasing to -1 m s^{-1} by 7 km. However, the Doppler velocity vertical gradient is weaker compared to that of the stratiform and mixed regime profiles. The main concentrations of Doppler velocity remain at -1 m s^{-1} above 7 km. The frequency distribution itself does not narrow with height above the freezing level, indicating that a significant number of convective profiles contained upper level downdrafts while the bulk of the profiles contained only the presence of falling ice and snow. The Doppler velocity spectrum from Manus Island (3.23b) shows a slightly different picture. This profile shows no significant change in values through the melting layer as in the NAME

case. Values at low levels reach –6 m s^{-1} below 4 km but the main concentration is near –2 m s^{-1}. Core values at upper levels vary between 0 and –1 m s^{-1}.

The spectral width frequency distribution associated with convective profiles is illustrated in Figure 3.20c. The distribution broadens with height. The distribution is centered at a width of 2 m s^{-1} near the surface and gradually increases to 3 m s^{-1} at 4 km. There are two visible main concentrations of frequency occurrence between 4 and 5 km. One concentration is centered at 3.5 m s^{-1} and associated with raindrops. The other is associated with frozen hydrometeors with a central value of 0.5 m s^{-1}. The distributions remain centered on 0.5 m s^{-1} above the melting layer with a significant frequency increase between 10 and 12 km. This indicates the lack of turbulent air motions within this layer. The Manus Island spectral width distributions (Figure 3.23c) are similar to those of NAME. The profile shows a trend of increasing values with height from the surface to 4 km and decreasing values with height above. However, values in the lowest 4 km are slightly lower compared to the NAME case, and values above 6 km are slightly higher than in the NAME case. The Manus Island distributions also show a gradual decrease in spectral width from 4 to 6 km, whereas the NAME profile shows a slight discontinuity.

The frequency distribution of convective vertical air motion shown in Figure 3.15d is broader below the melting layer than above it. The frequency spectrum ranges from –3 to 3 m s^{-1} in the lowest 2 km with a core value that weakens from –0.5 m s^{-1} near the surface to 0 m s^{-1} at 2 km. The distribution broadens from 2 to 4 km, revealing a noticeable updraft presence as strong as 10 m s^{-1}. A small, negative kink exists in the core of the distribution at 3 km where the vertical air motion decreases slightly. There

are multiple features within the melting layer. The distribution remains the same size but shifts in the negative direction. Between 4 and 5 km, the vertical air motion spectrum spans between –8 and 3 m s^{-1} with two cores of relatively high frequency occurrence at –1 and –4 m s^{-1}. The core at –4 m s^{-1} reveals that there was a high occurrence of mid-level downdrafts in the convective profiler cases. The vertical air motion becomes centered again at 0 m s^{-1} by 7 km. However, the vertical air motion spectrum broadens above 8 km due the weak presence of upper level updrafts and downdrafts on the order of 10 m s^{-1}.

The NAME convective vertical air motion composite was compared with convective composites from Darwin, Australia using a 50-MHz profiler, eastern Atlantic tropical oceanic squall lines using rawinsonde and aircraft data (Houze and Rappaport 1984; Gamache and Houze 1985), a West African tropical continental MCS using dual-Doppler radar analyses (Chong et al. 1983), a composite of tropical western Pacific island MCSs using wind profiler data (Balsley et al. 1988), and a mid-latitude MCS using dual-Doppler radar analyses (Biggerstaff and Houze 1993). These comparisons are displayed in Figure 3.24. All previous studies show upward motion throughout the depth of the troposphere, except near the tropopause. Two levels of maximum ascent are evident. The low-level peak is centered near 3 km and the second peak is centered in the middle troposphere. All three of the monsoon break MCSs were characterized by this bimodal updraft structure. While the low-level ascent is associated with convective elements forming along the leading edge of the convective line (drives warm rain coalescence processes), the upper level ascent peak is associated with deep, mature convective elements behind the leading edge of the squall line (Cifelli and Rutledge 1994). The

NAME profile also exhibits this bi-modal ascent structure. However, the profile shows descent between 4.5 and 7 km. The vertical air motion distributions from the western Amazon (Figure 3.25) span –10 to 13 m s^{-1}. The composite profiles show ascent through 15 km and no bimodal structure. The NAME composite is the only profile to show significant descent. This abnormal feature is dependent on multiple factors. The NAME composite is a mean profile from 749 individual convective profiles. The other composites are each based on a single MCS. The downward motion at mid levels in the NAME composite suggests that the 2875-MHz profiler observed stronger mid-level downdrafts than updrafts. However, the NAME composite may be biased towards downward motion due to both the hydrometeor identification algorithm and hydrometeor terminal fall speed interpolation technique used in this study. Any regions where the hydrometeor identification algorithm failed to identify hail and instead identified graupel were likely to contain underestimations in hydrometeor terminal fall speeds, and thus in the vertical air motion estimates. The vertical air motion estimates in the melting layer were based on interpolations rather than independent estimations at every level. This creates uncertainty in the vertical air motion estimates as well.

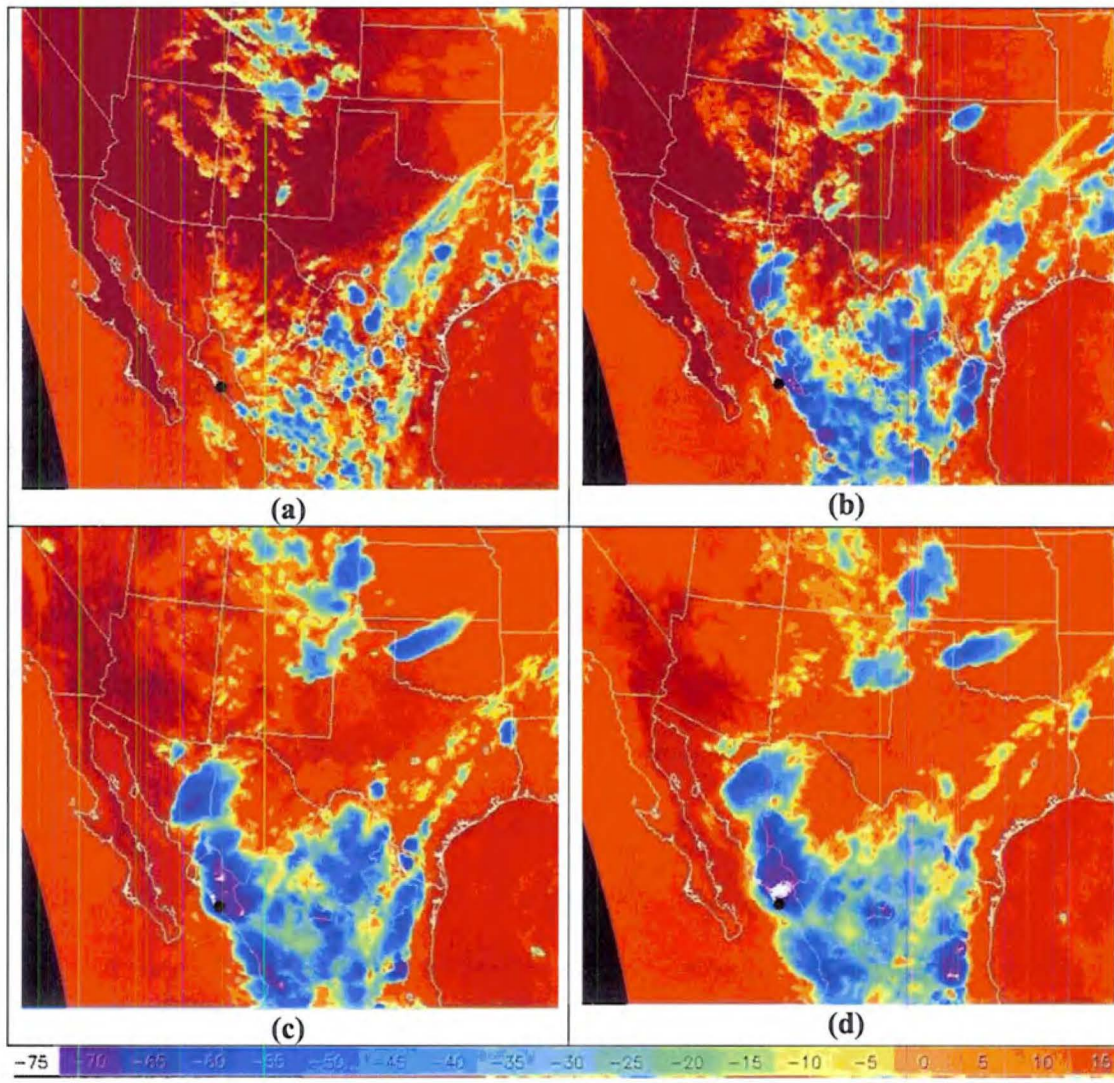

Figure 3.1: Infrared satellite images centered over the NAME region for 30-31 July 2004: (a) 2015 UTC (b) 2315 UTC (c) 0145 UTC and (d) 0345 UTC. Contoured temperature is in units of degrees Celsius. The approximate location of the NOAA profiler site is marked with a black dot (from the UCAR online weather archive: http://locust.mmm.ucar.edu/case-selection/).

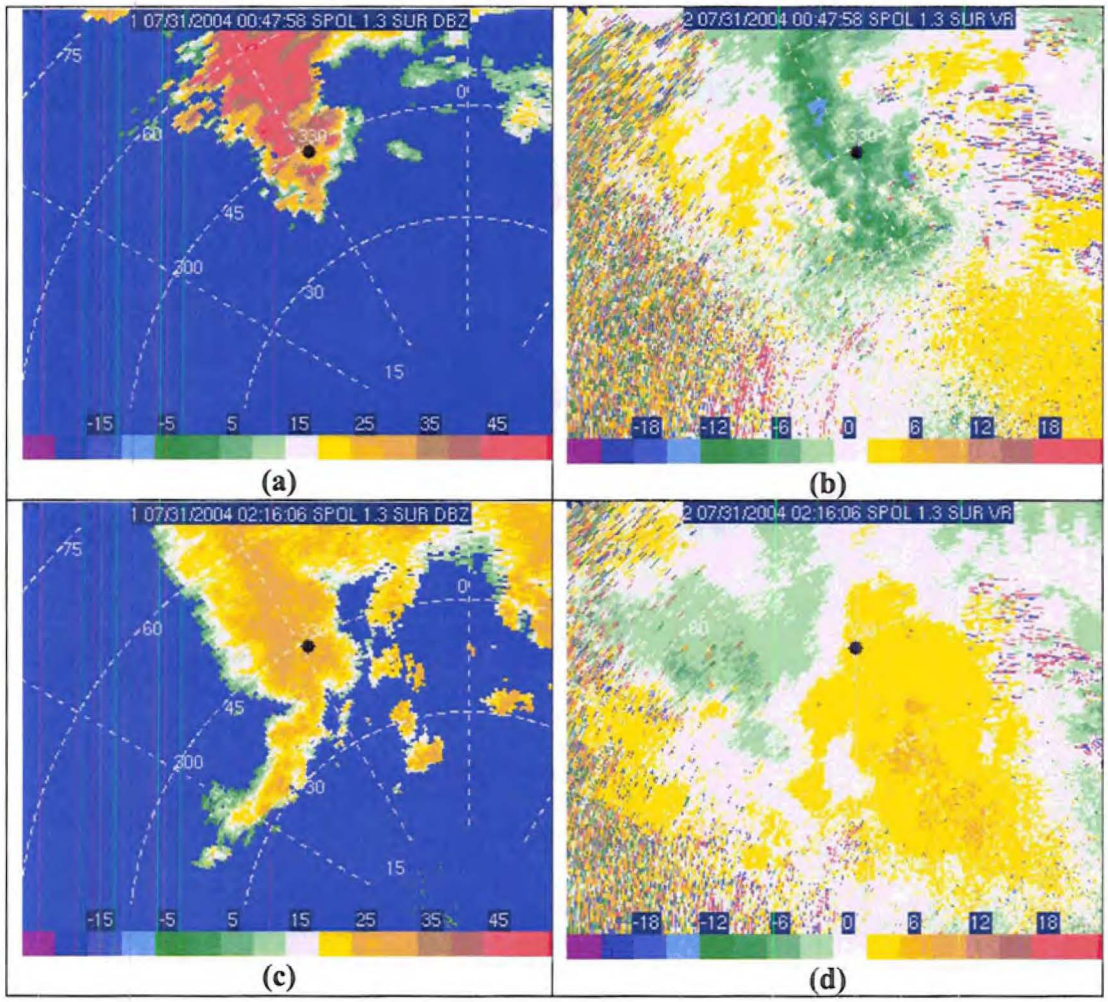

Figure 3.2: S-Pol images of precipitation at 1.3° elevation angle over the NOAA profiler site (331.65° azimuth, 44.42 km range) on 31 July 2004. Panels (a) and (b) show reflectivity (dBZ) and mean Doppler velocity (m s^{-1}), respectively, at 00:47:58 UTC. Panels (c) and (d) show reflectivity and mean Doppler velocity, respectively, at 02:16:06 UTC. The profiler location is marked by a black dot in each panel.

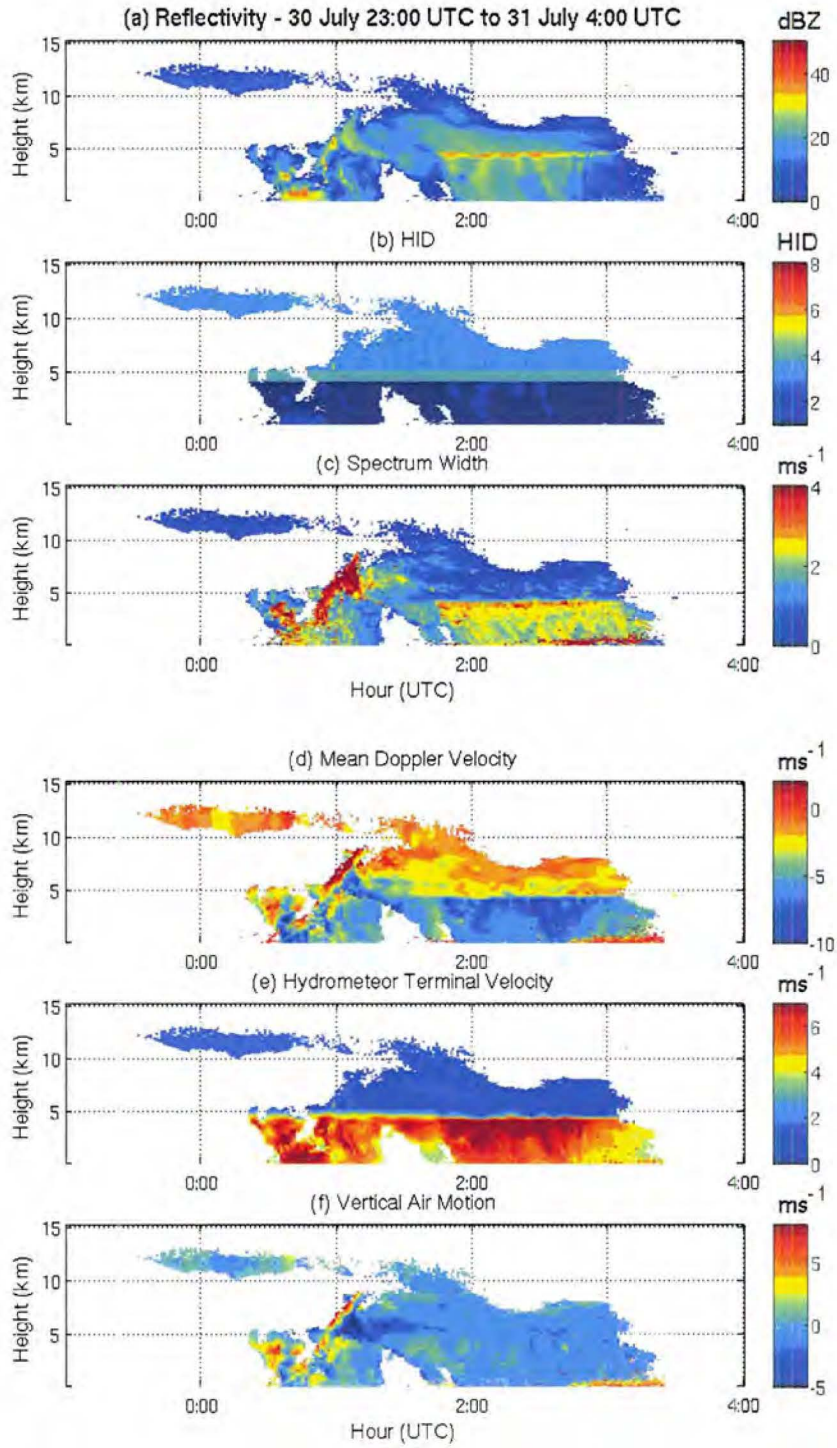

Figure 3.3: Time versus height contour plots of (a) reflectivity (b) HID (c) spectral width (d) mean Doppler velocity (e) hydrometeor terminal fall velocity and (f) vertical air motion for the 30-31 July 2004 rainfall event from the 2875-MHz profiler.

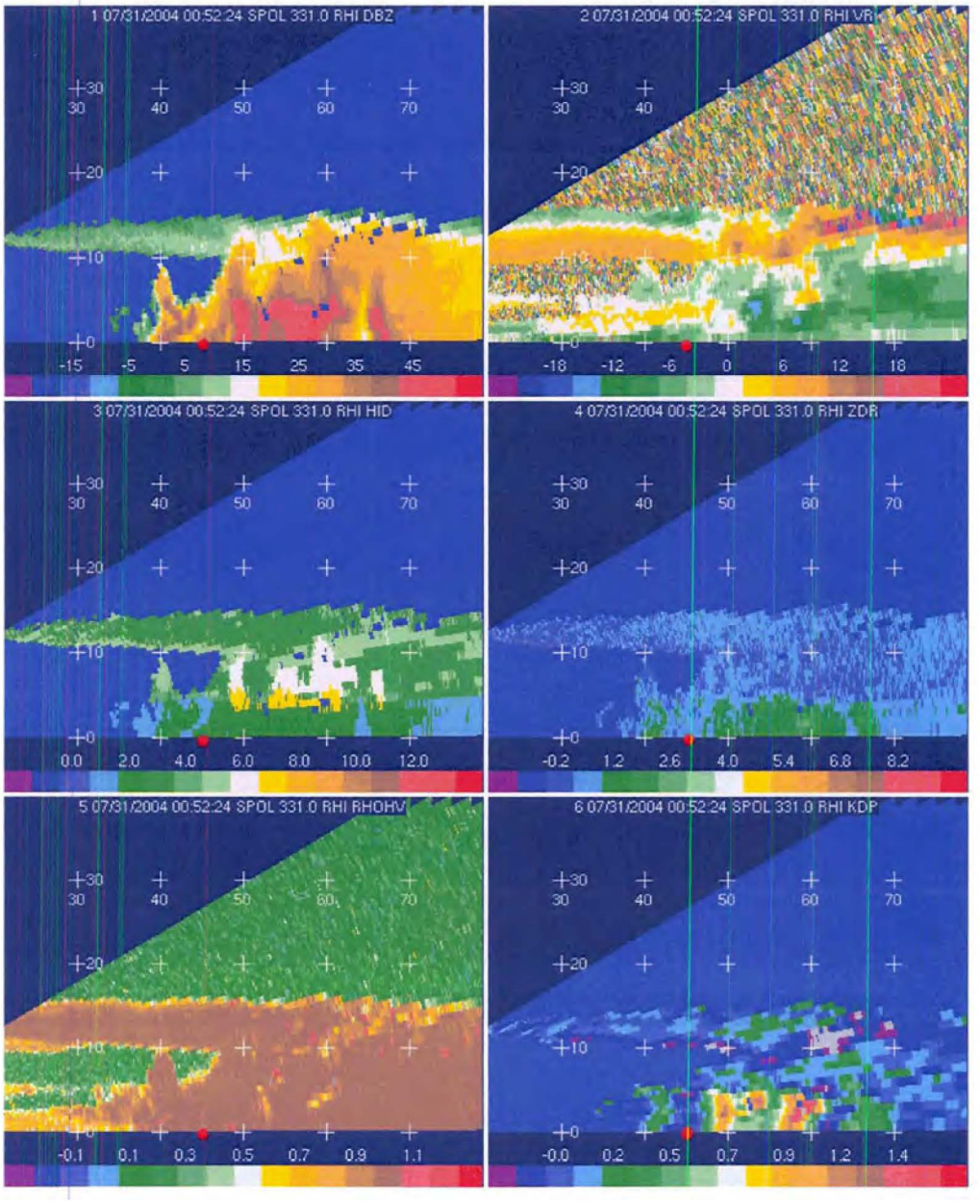

Figure 3.4: S-Pol RHI taken over the NOAA profiler site (331° azimuth) at 00:52:24 UTC on 31 July 2004. The radar variables displayed include reflectivity in dBZ (upper left), mean radial velocity in m s^{-1} (upper right), HID (middle left), Z_{dr} in dB (middle right), ρ_{hv} (bottom left), and K_{dp} in deg km^{-1} (bottom right). Range is labeled at the top of each panel from 30 to 70 km. The range of the profiler site is marked as a red dot in each panel.

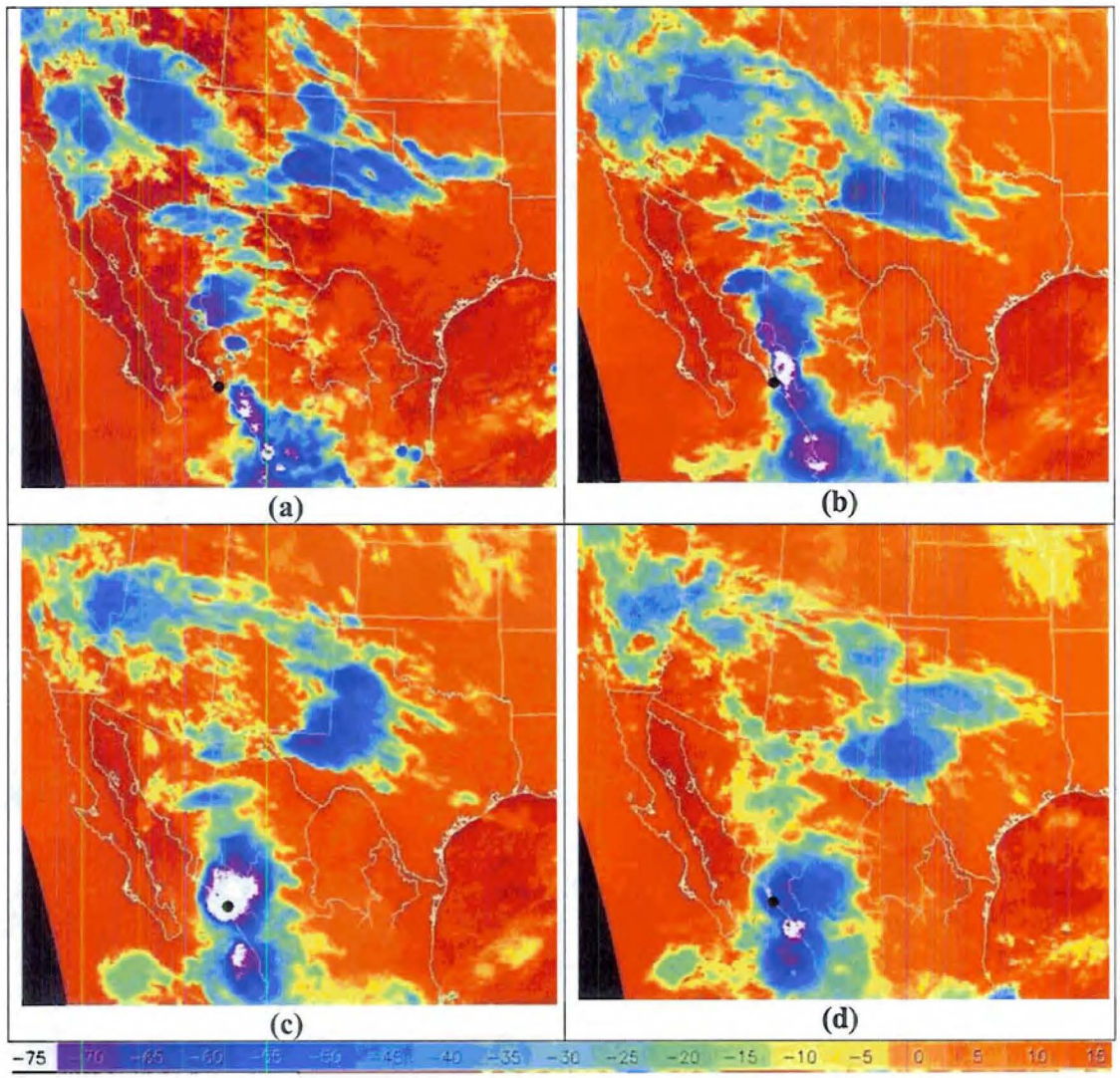

Figure 3.5: Infrared satellite images centered over the NAME region for 13 August 2004: (a) 0045 UTC (b) 0345 UTC (c) 0645 UTC and (d) 0915 UTC. Contoured temperature is in units of degrees Celsius. The approximate location of the NOAA profiler site is marked with a black dot (from the UCAR online weather archive: http://locust.mmm.ucar.edu/case-selection/).

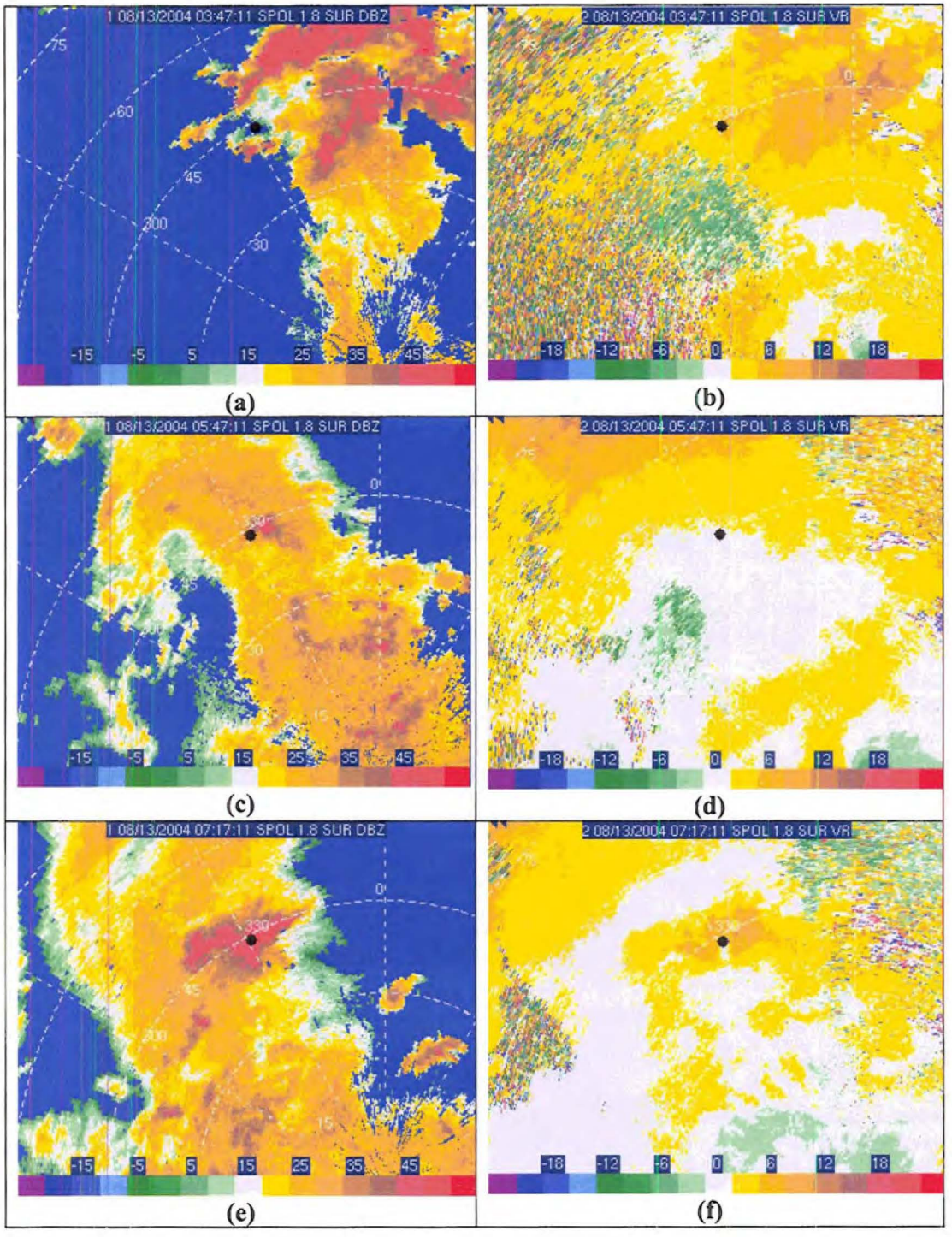

Figure 3.6: S-Pol images of precipitation at 1.8° elevation angle over the NOAA profiler site (331.65° azimuth, 44.42 km range) on 13 August 2004. Left panels display reflectivity (dBZ) and right panels display mean Doppler velocity (m s^{-1}). The top panels are for 03:47:11 UTC. The middle panels are for 05:47:11 UTC, and the bottom panels are for 07:17:11 UTC. The profiler site is marked as a black dot in each panel.

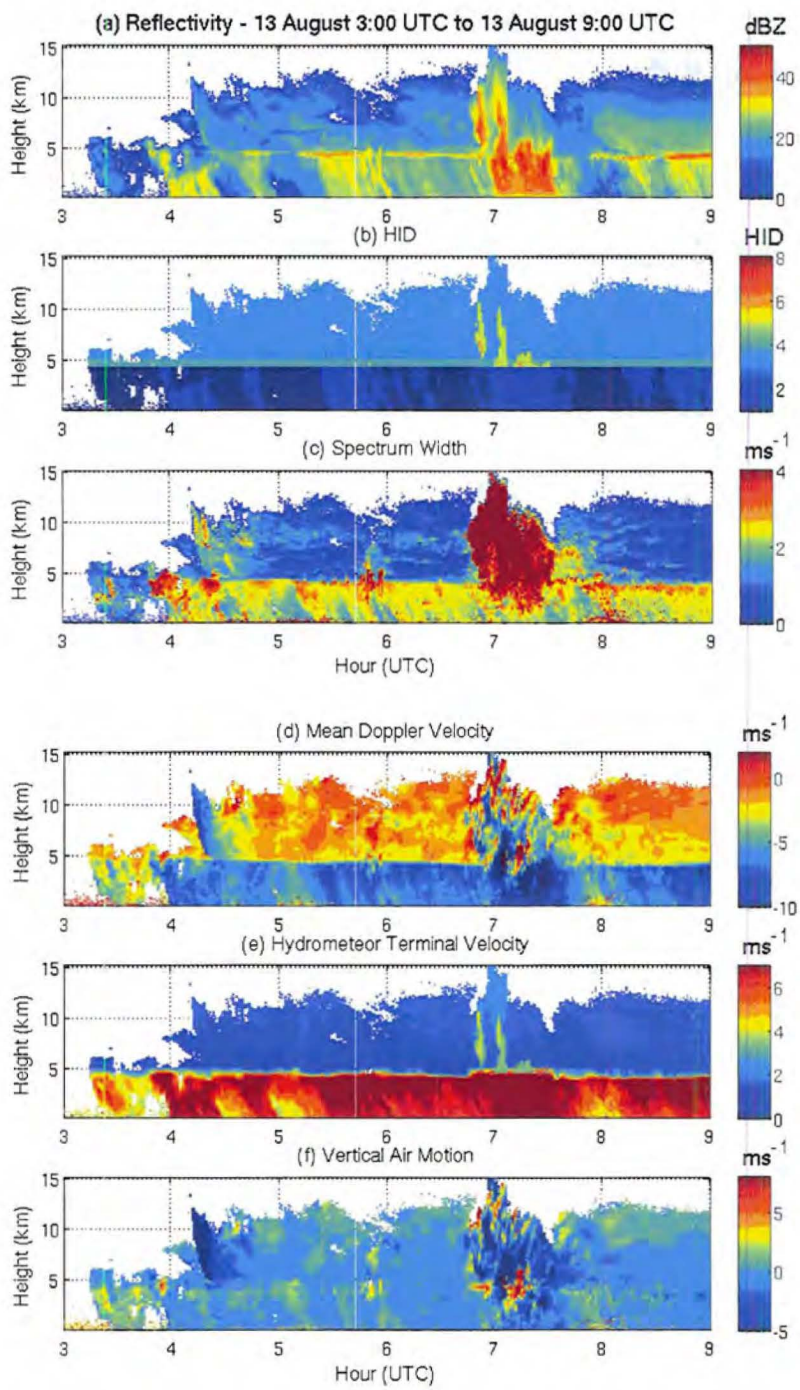

Figure 3.7: Time versus height contour plots of (a) reflectivity (b) HID (c) spectral width (d) mean Doppler velocity (e) hydrometeor terminal fall velocity and (f) vertical air motion for the 13 August 2004 rainfall event from the 2875-MHz profiler. Note that for Doppler velocity and vertical air motion plots, upward motions are positive and downward motions are negative. The hydrometeor terminal velocities are presented as absolute (positive) values, representing downward motions.

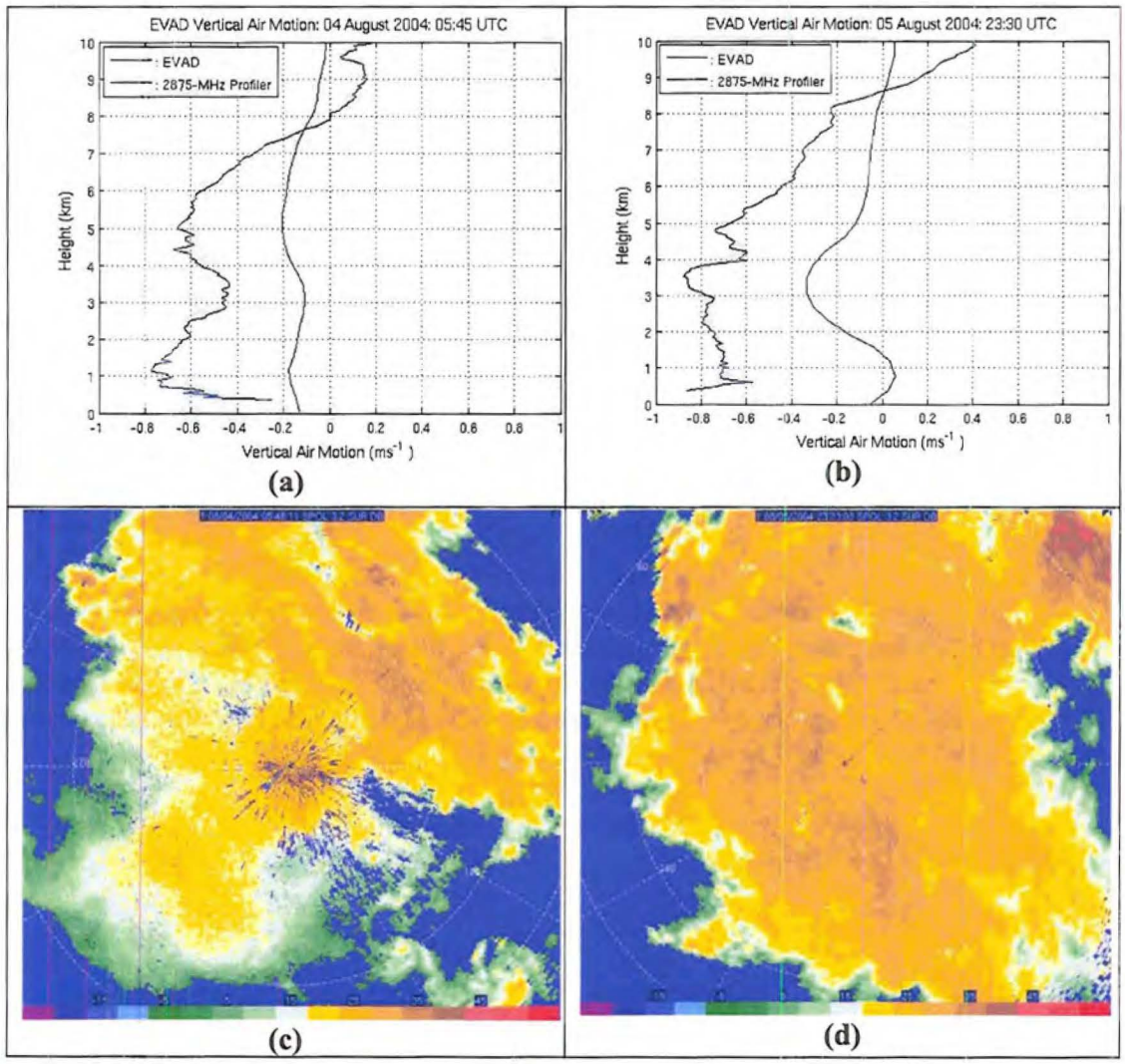

Figure 3.8: EVAD results for 4-5 August 2004. The top panels show profiles of mean vertical air motion from both the EVAD technique (black) and the 2875-MHz profiler (blue). The lower panels display PPI images of S-Pol reflectivity at 3.2° elevation angle. The left panels are plots of the 4 August case at 0545 UTC and the right panels are of the 5 August case at 2330 UTC.

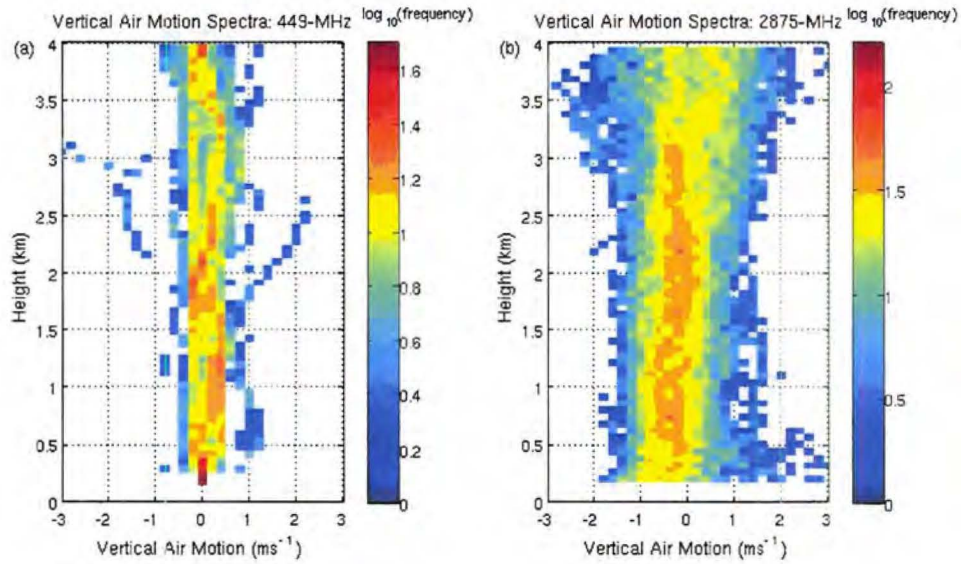

Figure 3.9: Frequency distributions profiles of derived vertical air motion in stratiform precipitation during the 13 August 2004 precipitation event for both the (a) 449-MHz profiler and (b) 2875-MHz profiler. Note that due to the different temporal resolution between profilers, the 449-MHz profiler spectra plot is based on 75 profiles while that of the 2875-MHz profiler is based on 252 profiles.

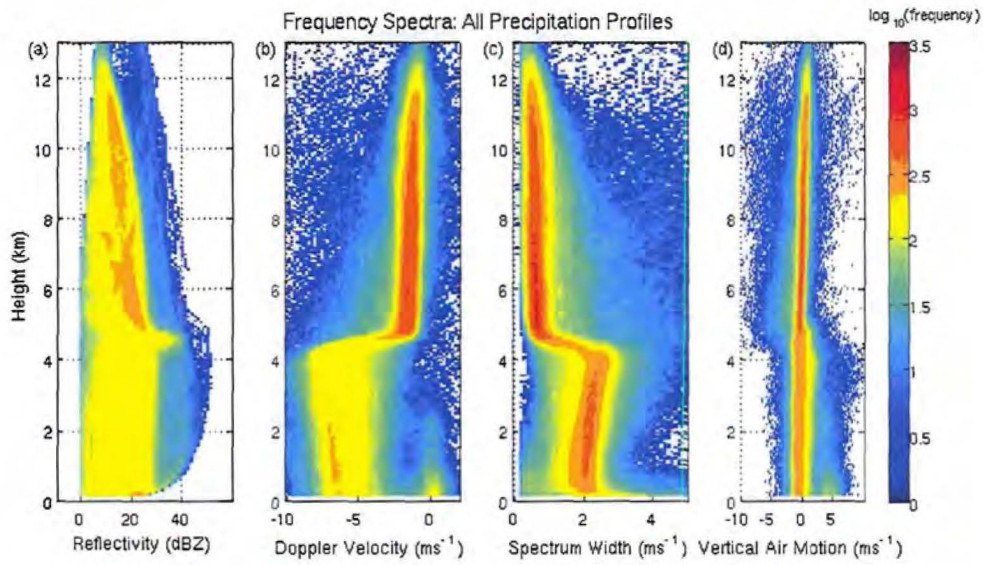

Figure 3.10: Frequency distribution profiles of (a) reflectivity (b) mean Doppler velocity (c) spectral width and (d) vertical air motion for the entire 2875-MHz profiler NAME dataset. All variables are contoured in log base 10 of the frequency occurrence.

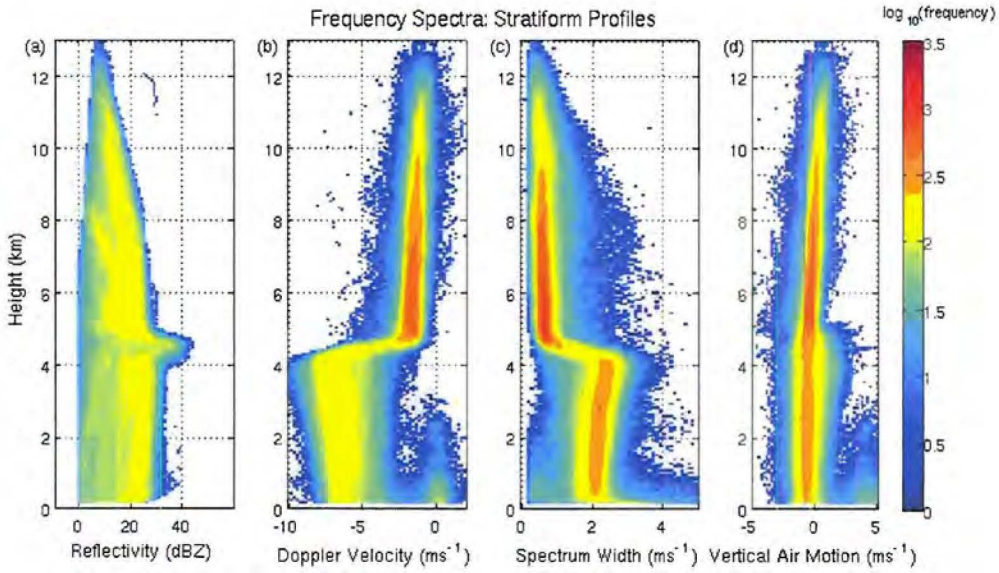

Figure 3.11: Frequency distribution profiles of (a) reflectivity (b) mean Doppler velocity (c) spectral width and (d) vertical air motion for the 2875-MHz stratiform NAME profiles. All variables are contoured in log base 10 of the frequency occurrence.

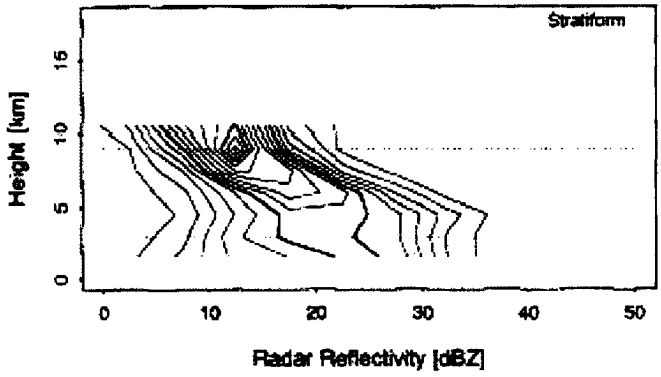

Figure 3.12: Climatological CFAD of radar reflectivity for the volume scans collected at 6-hour intervals during February 1988 by the operational radar at Darwin, Australia. CFAD bin size is 5 dBZ. The contours are at intervals of 0.5 % of data per kilometer, starting with the 0.5 % dBZ^{-1} km^{-1} contour. The 3 % and 6 % dBZ^{-1} km^{-1} contours are highlighted. Note that the CFAD has been truncated at the altitude where the number of points (per height level) drops below 10 % of the maximum number of points at any level. This CFAD is based on stratiform radar echoes only (From Steiner et al. 1995).

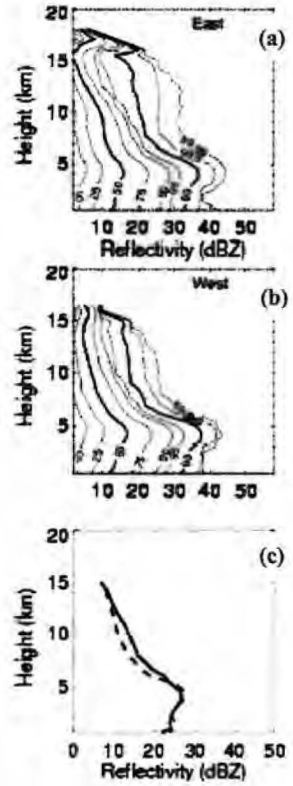

Figure 3.13: TRMM-LBA S-Pol reflectivity climatologic results of stratiform precipitation from the western Amazon during January and February of 1999. The upper two panels depict cumulative frequency distributions of radar reflectivity for (a) the east regime and (b) the west regime. The 50 % and 99 % contours are highlighted. Figure 3.13c depicts mean radar reflectivity for the east (solid) and west (dashed) regimes. The cumulative frequency distributions were constructed using a 4-dB bin size and 15 total bins (Adapted from Cifelli et al. 2004).

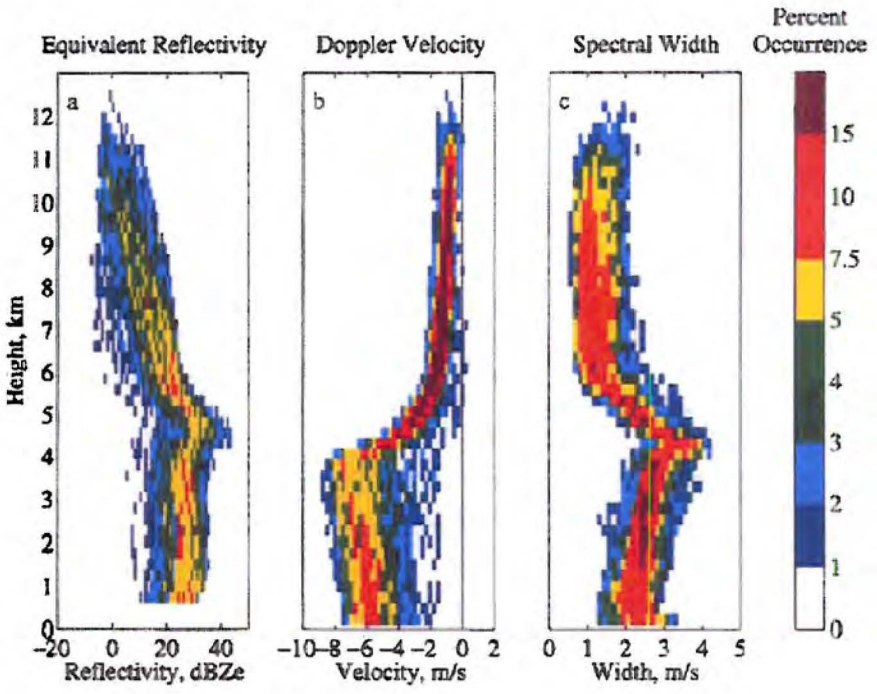

Figure 3.14: Frequency distribution of spectral moments for all hours of surface detected stratiform rain at Manus Island from May 1992 through February 1993, (a) Equivalent reflectivity, (b) Doppler velocity, and (c) spectral width (From Williams et al. 1995).

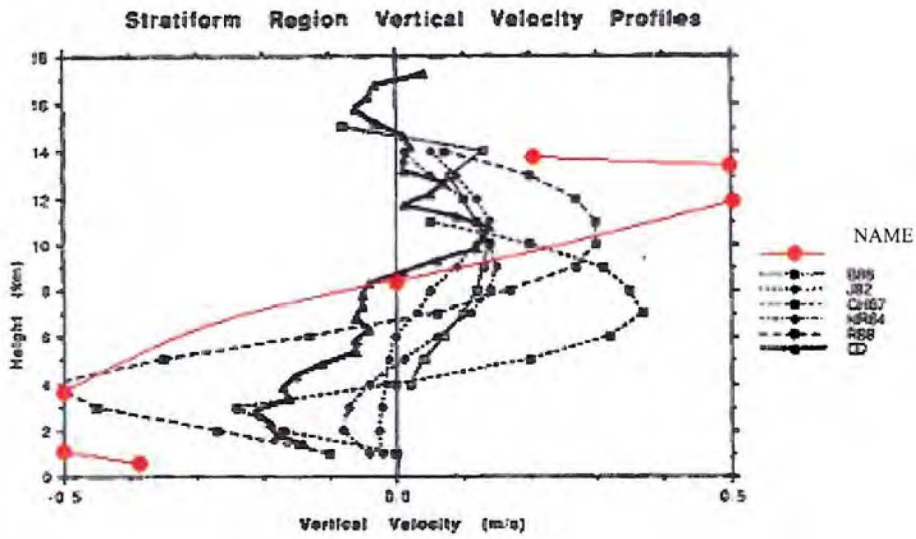

Figure 3.15: Comparison of stratiform region vertical air motion profiles: Symbols in the legend refer to the following: B88 for Balsley et al. (1988); J82 for Johnson (1982); CH87 for Chong et al. (1987); HR84 for Houze and Rappaport (1984); R88 for Rutledge et al. (1988); DD for Cifelli and Rutledge (1994); and NAME for the results of this study (red). Note that widely different sample sizes and temporal and spatial averaging go into the various curves of this figure (Adapted from Cifelli and Rutledge 1994).

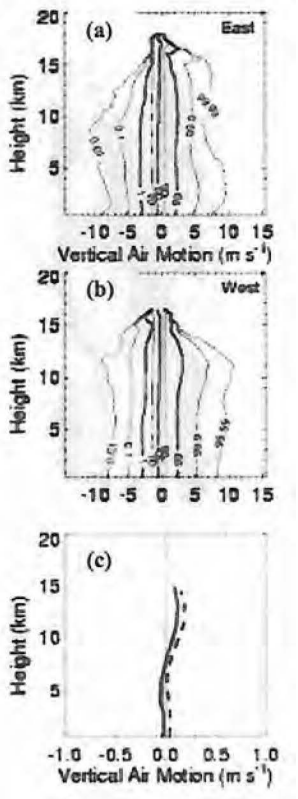

Figure 3.16: TRMM-LBA S-Pol vertical air motion climatologic results of stratiform precipitation from the western Amazon during January and February of 1999. The upper two panels depict cumulative frequency distributions of vertical air motion for (a) the east regime and (b) the west regime. The 1 %, 50 %, and 99 % contours are highlighted. Figure 3.13c depicts mean vertical air motion for the east (solid) and west (dashed) regimes. The cumulative frequency distributions were constructed using a 1.0 m s^{-1} bin size and 31 total bins (Adapted from Cifelli et al. 2004).

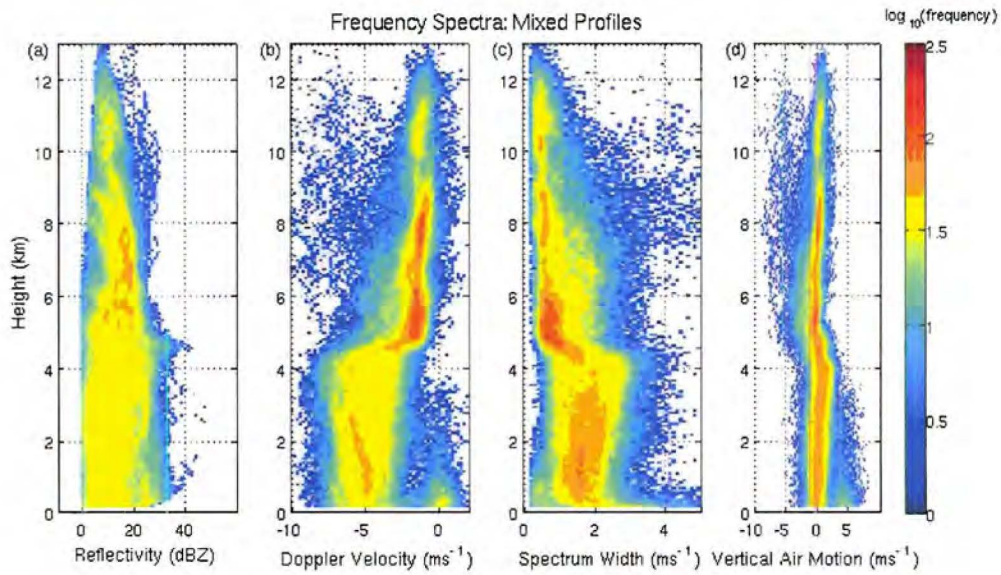

Figure 3.17: Frequency distribution profiles of (a) reflectivity (b) mean Doppler velocity (c) spectral width and (d) vertical air motion for the 2875-MHz mixed stratiform/convective NAME profiles. All variables are contoured in log base 10 of the frequency occurrence.

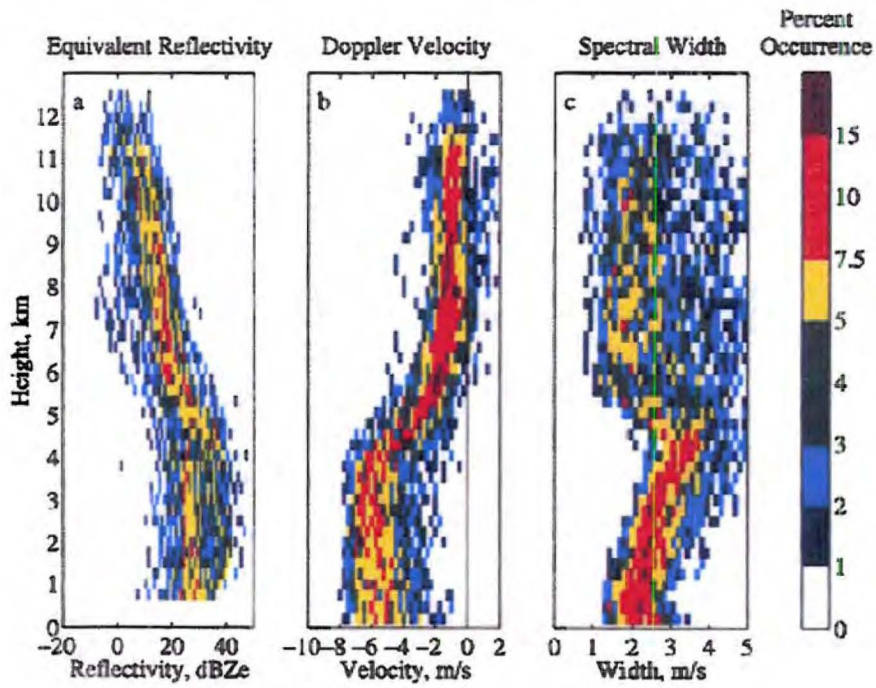

Figure 3.18: Frequency distribution of spectral moments for all hours of surface detected mixed stratiform/convective rain at Manus Island from May 1992 through February 1993, (a) Equivalent reflectivity, (b) Doppler velocity, and (c) spectral width (From Williams et al. 1995).

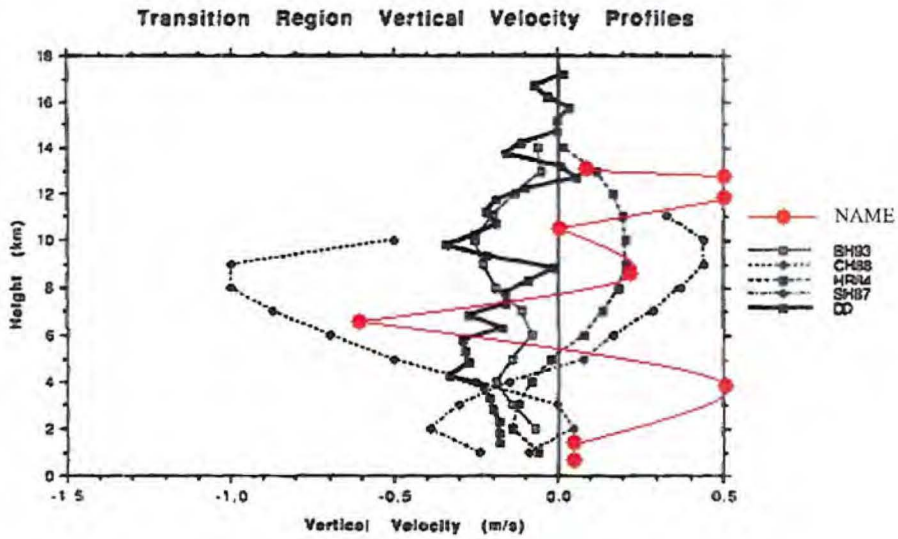

Figure 3.19: Comparison of transition (mixed) region vertical air motion profiles: Symbols in the legend refer to the following: BH93 for Biggerstaff and Houze (1993); CH88 for Chalon et al. (1988); HR84 for Houze and Rappaport (1984); SH87 for Smull and Houze (1987); DD for Cifelli and Rutledge (1994); and NAME for the results of this study (red). Note that widely different sample sizes and temporal and spatial averaging go into the various curves of this figure (Adapted from Cifelli and Rutledge 1994).

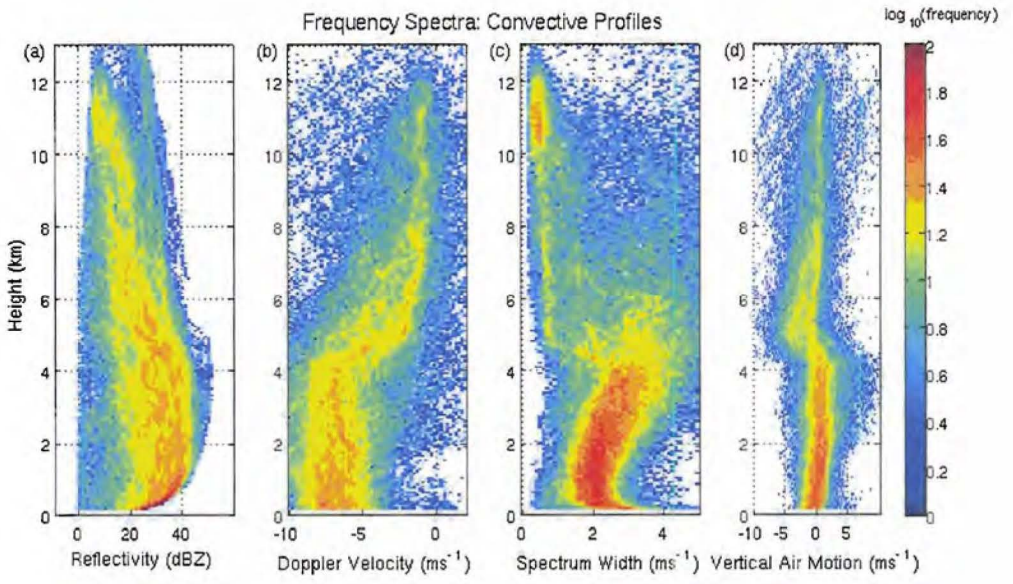

Figure 3.20: Frequency distribution profiles of (a) reflectivity (b) mean Doppler velocity (c) spectral width and (d) vertical air motion for the 2875-MHz convective NAME profiles. All variables are contoured in log base 10 of the frequency occurrence.

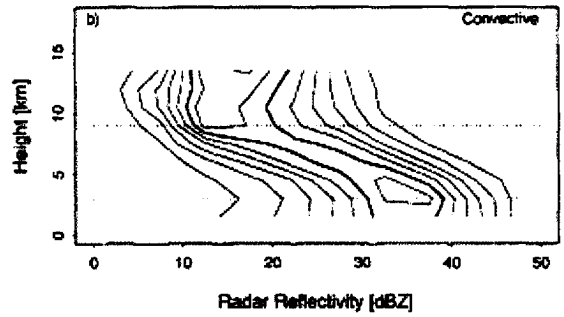

Figure 3.21: Climatological CFAD of radar reflectivity for the volume scans collected at 6-hour intervals during February 1988 by the operational radar at Darwin, Australia. CFAD bin size is 5 dBZ. The contours are at intervals of 0.5 % of data per kilometer, starting with the 0.5 % dBZ^{-1} km^{-1} contour. The 3 % and 6 % dBZ^{-1} km^{-1} contours are highlighted. Note that the CFAD has been truncated at the altitude where the number of points (per height level) drops below 10 % of the maximum number of points at any level. This CFAD is based on convective radar echoes only (From Steiner et al. 1995).

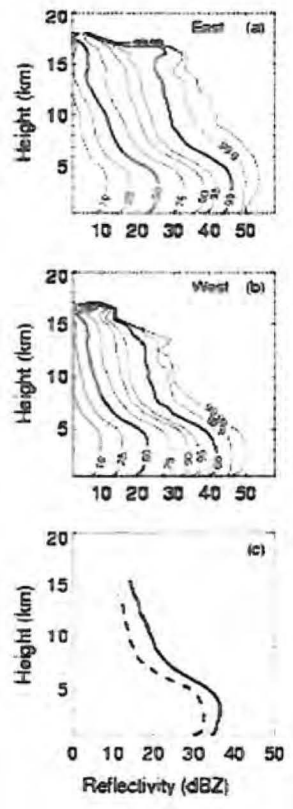

Figure 3.22: TRMM-LBA S-Pol reflectivity climatologic results of convective precipitation from the western Amazon during January and February of 1999. The upper two panels depict cumulative frequency distributions of radar reflectivity for (a) the east regime and (b) the west regime. The 50 % and 99 % contours are highlighted. Figure 3.13c depicts mean radar reflectivity for the east (solid) and west (dashed) regimes. The cumulative frequency distributions were constructed using a 4-dB bin size and 15 total bins (From Cifelli et al. 2004).

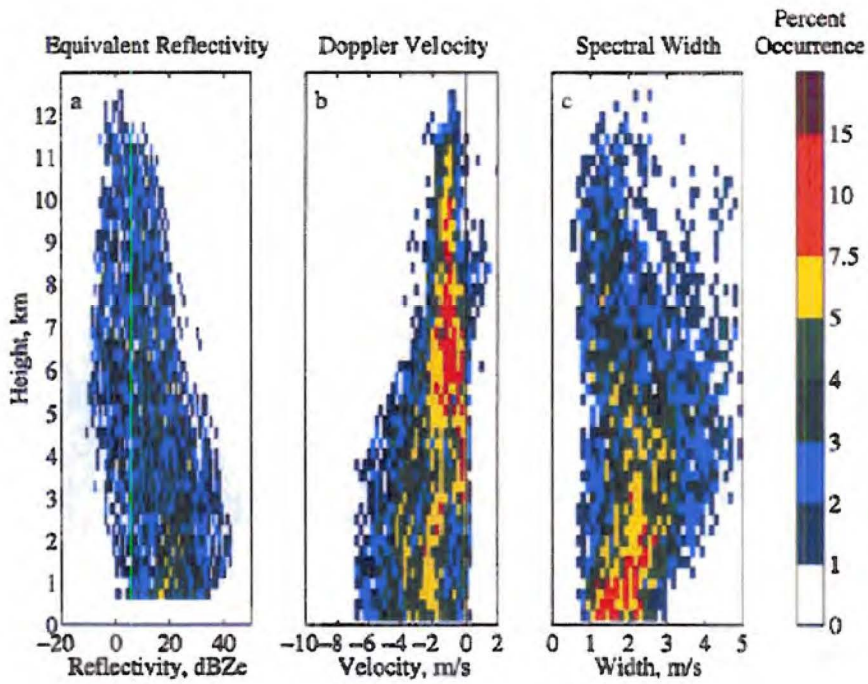

Figure 3.23: Frequency distribution of spectral moments for all hours of surface detected convective rain at Manus Island from May 1992 through February 1993, (a) Equivalent reflectivity, (b) Doppler velocity, and (c) spectral width (From Williams et al. 1995).

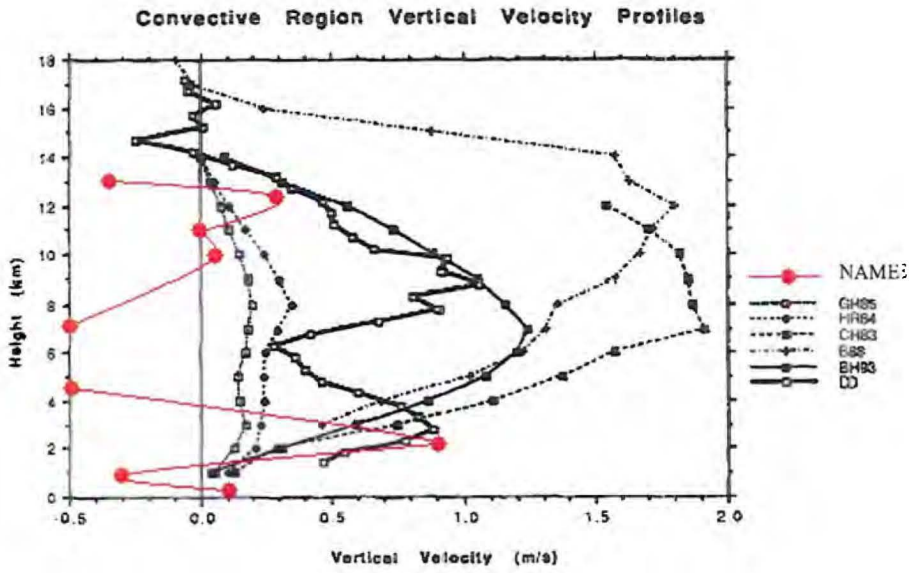

Figure 3.24: Comparison of convective region vertical air motion profiles: Symbols in the legend refer to the following: GH85 for Gamache and Houze (1985); HR84 for Houze and Rappaport (1984); CH83 for Chong et al. (1983) [adapted from Houze (1989)]; B88 for Balsley et al. (1988); BH93 for Biggerstaff and Houze (1993); DD for Cifelli and Rutledge (1994); and NAME for the results of this study (red). Note that widely different sample sizes and temporal and spatial averaging go into the various curves of this figure (Adapted from Cifelli and Rutledge 1994).

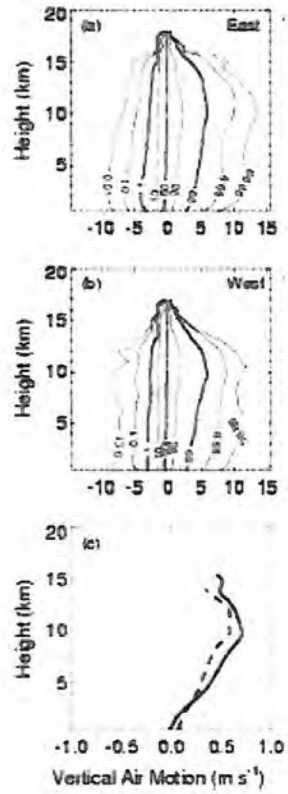

Figure 3.25: TRMM-LBA S-Pol vertical air motion climatologic results of convective precipitation from the western Amazon during January and February of 1999. The upper two panels depict cumulative frequency distributions of vertical air motion for (a) the east regime and (b) the west regime. The 1 %, 50 %, and 99 % contours are highlighted. Figure 3.13c depicts mean vertical air motion for the east (solid) and west (dashed) regimes. The cumulative frequency distributions were constructed using a 1.0 m s^{-1} bin size and 31 total bins (Adapted from Cifelli et al. 2004).

CHAPTER 4

Conclusions and Future Work

4.1 Conclusions

The primary focus of this study was to create a climatology of the vertical structure of precipitating cloud systems during the NAME field campaign. This vertical structure is important in understanding how the distribution of latent heating affects the atmospheric circulation and how to better parameterize precipitating cloud systems in numerical models (Williams et al. 1995). The vertical structure of these precipitating clouds was analyzed using reflectivity, Doppler velocity, and spectral width derived from the vertically pointing 2875-MHz profiler radar that was stationed near Sinaloa, Mexico during the summer and early fall of 2004. The precipitating clouds were classified as either stratiform, mixed stratiform/convective, or convective clouds. Vertical air motions were estimated using the dataset, because the vertical distribution of heating in tropical precipitation is dominated by contributions involving phase changes of water (Houze 1989), which are in turn proportional to vertical air motion profiles (Cifelli and Rutledge 1994). The derived vertical air motions were compared with both EVAD and 449-MHz profiler retrievals, and it was found that the 2875-MHz profiler vertical air motion estimates contained a negative bias to both methods of approximately 0.5 m s^{-1}. While the errors in the stratiform vertical air motion estimates were of the same order as the stratiform air motions, the 2875-MHz profiler results proved useful in analyzing the vertical structure of vertical air motion for various precipitation regimes in a mean sense

as well as assessing general updraft and downdraft intensity in convective precipitation.

Two case studies were presented and reaffirmed the study by Lang et al. (2005) that found MCSs to be the dominant form of convection within the NAME Tier-I domain. These studies found that stratiform precipitation exhibited a radar bright band and a strong Doppler velocity gradient in the melting layer, and weak spectral width above the melting layer. Mixed stratiform/convective regions contained low reflectivity, weak ascent at upper levels, and weak ascent just below the melting layer. Convective profiles were dominated by updrafts and downdrafts on the order of 10 m s^{-1}.

The 23 cases recorded during NAME by the 2875-MHz profiler were dominated by stratiform precipitation. However, both the onsite rain gauge- and S-Pol-based rainfall estimations showed that surface rainfall was primarily accumulated from convective precipitation, due to associated convective rainfall rates that were significantly higher than those from stratiform and mixed rainfall. Frequency distributions of reflectivity, Doppler velocity, and spectral width were created for the various precipitation regimes. The NAME distributions compared favorably with those from Manus Island, Papua New Guinea (Williams et al. 1995), Darwin, Australia (Steiner et al. 1995), and the western Amazon in Brazil (Cifelli et al. 2004).

NAME vertical air motion composites were created for stratiform, mixed stratiform/convective, and convective precipitation. These composites were compared with previous studies described by Cifelli and Rutledge (1994) along with composites from the western Amazon (Cifelli et al. 2004). The NAME stratiform and mixed stratiform/convective composites exhibited similar features to the composites of the previous studies. However, convective composites from past studies showed ascent

throughout the troposphere, and the NAME composite showed a significant region of descent between 4 and 6 km. While this discrepancy can primarily be explained by the 2875-MHz profiler negative bias of 0.5 m s^{-1}, it shows that there may have been a problem with the interpolation method used in estimating vertical air motions within the melting layer.

4.2 Future Work

Improvements can be made to the methodology used in this study to determine the terminal fall velocities of raindrops. This study utilized mean normalized drop size distribution variables, N_w and μ, derived from the 13 August rain event. These variables should be estimated on a case-by-case basis rather than for just a single rain event (assumed to be representative of all events) to reduce the existing negative bias in the vertical air motion estimates. The 2875-MHz profiler vertical air motion estimates derived in this study also contained minor discontinuities at the melting layer boundaries. In future studies, it would be beneficial to determine a method for estimating hydrometeor terminal fall speeds in the melting layer directly instead of using interpolation techniques.

Future work includes separating the profiles classified as convective clouds into shallow convective and deep convective regimes, where shallow convective profiles contain no hydrometeors above the melting level. The latent heat associated with freezing and melting of water is important in the dynamical forcing of the atmosphere, and the separation of clouds with and without these processes may be important for cloud parameterization in atmospheric models (Williams et al. 1995). Once the 2875-MHz

profiler dataset is robust, the final step will include creating vertical profiles of apparent heat source (Q_1; Yanai et al. 1973) for the various precipitation regimes following the methodology of Cifelli and Rutledge (1998).

REFERENCES

Ackerman, T. P., K. N. Liou, F. P. J. Valero, and L. Pfister, 1988: Heating rates in tropical anvils. *J. Atmos. Sci.*, **45**, 1606–1622.

Adams, D. K., and A. C. Comrie, 1997: The North American Monsoon. *Bull. Amer. Met. Soc.*, **78**, 2197–2213.

Atlas, D., and C. R. Williams, 2003: The anatomy of a continental Tropical convective storm. *J. Atmos. Sci.*, **60**, 3-15.

Atlas, D., R. C. Srivastava and R. S. Sekhon, 1973: Doppler radar characteristics of precipitation at vertical incidence. *Rev. Geophys. Space Phys.*, **11**, 1-35.

Atlas, D., C. W. Ulbrich, and C. R. Williams, 2004: Physical origin of a wet microburst: Observations and theory. *J. Atmos. Sci.*, **61**, 1186-1195.

Balsley, B. B., W. L. Ecklund, D. A. Carter, A. C. Riddle, and K. S. Gage, 1988: Average vertical motions in the tropical atmosphere observed by a radar wind profiler on Pohnpei (7°N latitude, 157°E longitude). *J. Atmos. Sci.* , **45**, 396-405.

Beard, K.V. and Chuang, C., 1987: A new model for the equilibrium shape of raindrops, *J. Atmos. Sci.,* **44**, 1509-1524.

Beard, K. V., 1985: Simple Altitude Adjustments to Raindrop Velocities for Doppler Radar Analysis. *J. Atmos. Oceanic Tech.*, **2**, 468–471.

Biggerstaff, M. I., and R. A. Houze, Jr., 1993: Kinematics and microphysics of the transition zone of the 10-11 June 1985 squall line. *J. Atmos. Sci.*, **50**, 3091-3110.

Bringi, V.N., and V. Chandrasekar, 2001: Polarimetric Doppler Weather Radar: Principles and Applications, Cambridge University Press, Cambridge, United Kingdom, 636 pp.

Browning, K. A., and R. Wexler, 1968: The Determination of Kinematic Properties of a Wind Field Using Doppler Radar. *J. App. Meteor.*, **7**, 105–113.

Carey, L. D., and S. A. Rutledge, 1996: A multiparameter radar case study of the microphysical and kinematic evolution of a lightning producing storm. *Meteor. Atmos. Phys.*, **59**, 33-64.

Carey, L. D., S. A. Rutledge, D. A. Ahijevych, and T. D. Keenan, 2000: Correcting propagation effects in C-Band polarimetric radar observations of tropical convection using differential propagation phase. *J. Appl. Meteorol.*, **39**, 1405–1433.

Caton, P. G. F., 1963: The measurement of wind and convergence by Doppler radar. *Proceedings, 10th Weather Radar Conference*, Washington, D.C., Amer. Meteor. Soc., 290-296.

Chalon, J. P., G. Jaubert, F. Roux, and J. P. Lafore, 1988: The West African squall line observed on 23 June 1981 during COPT 81: Mesoscale structure and transports. *J. Atmos. Sci.*, **45**, 2744-2763.

Chandrasekar, V., Bringi, V. N., Balakrishnan, N., and D. S. Zrnic, 1990: Error structure of multiparameter radar and surface measurements of rainfall. Part III: Specific differential phase. *J. Atmos. Oceanic Tech.*, **7**, 621-629.

Cheng, M., and C. G. Collier, 1993: An Objective Method for Recognizing and Partially Correcting Brightband Error in Radar Images. *J. App. Met.*, **32**, 1142–1149.

Chong, M., J. Testud, and F. Roux, 1983: Three-dimensional wind field analysis from dual-Doppler radar data. Part II: Minimizing the error due to temporal variation. *J. Climate Appl. Meteor.*, **22**, 1216-1226.

Chong, M., P. Amayenc, G. Scialom, and J. Testud, 1987: A tropical squall line observed during the COPT 81 experiment in West Africa. Part I: Kinematic structure inferred from dual-Doppler radar data. *Mon. Wea. Rev.*, **115**, 670-694.

Cifelli, R. and S. A. Rutledge, 1994: Vertical Motion Structure in Maritime continent mesoscale Convective Systems: Results from a 50-MHz Profiler. *J. Atmos. Sci.*, **51**, 2631-2652

Cifelli, R., and S. A. Rutledge, 1998: Vertical motion, diabatic heating, and rainfall characteristics in N. Australia convective systems. *Quart. J. Roy. Meteor. Soc.*, **124**, 1133–1162.

Cifelli, R., L. Carey, W. A. Petersen, and S. A. Rutledge, 2004: An Ensemble Study of Wet Season Convection in Southwest Amazonia: Kinematics and Implications for Diabatic Heating. *J. Climate*, **17**, 4692-4707.

Cifelli, R., S. A. Rutledge, D. J. Boccippio, and T. Matejka, 1996: Horizontal Divergence and Vertical Velocity Retrievals from Doppler Radar and Wind Profiler Observations. *J. Atmos. Oceanic Tech.*, **13**, 948–966.

Douglas, M. W., R. Maddox, K. Howard, and S. Reyes, 1993: The Mexican monsoon. *J. Climate*, **6**, 1665–1667.

Doviak, R. J., and D. S. Zrnic, 1993: Doppler Radar and Weather Observations, 2nd Ed., Academic Press, San Diego, California, 562 pp.

Ecklund, W. L., C. R. Williams, P. E. Johnston, and Kenneth S. Gage, 1999: A 3-GHz profiler for precipitating cloud studies. *J. Atmos. Oceanic Tech.*, **16**, 309–322.

Gamache, J. F., and R. A. Houze Jr., 1985: Further analysis of the composite wind and thermodynamic structure of the 12 September GATE squall line. *Mon. Wea. Rev.*, **113**, 1241-1259.

Gochis, D. J., A. Jimenez, C. J. Watts, J. Garatuza-Payan and W. J. Shuttleworth, 2004: Analysis of 2002 and 2003 warm-season precipitation from the North American Monsoon Experiment event rain gauge network. *Mon. Wea. Rev.*, **132**, 2938–2953.

Gochis, D. J., W. J. Shuttleworth, and Zong-Liang Yang, 2003: Hydrometeorological response of the modeled North American monsoon to convective parameterization. *J. Hydromet.*, **4**, 235–250.

Hartmann, D. L., H. H. Hendon, and R. A. Houze Jr., 1984: Some implications of the mesoscale circulations in tropical cloud clusters for large-scale dynamics and climate. *J. Atmos. Sci.*, **41**, 113–121.

Higgins, W., D. Ahijevych, J. Amador, A. Barros, E. H. Berbery, E. Caetano, R. Carbone, P. Ciesielski, R. Cifelli, M. Cortez-Vazquez, A. Douglas, M. Douglas, G. Emmanuel, C. Fairall, D. Gochis, D. Gutzler, T. Jackson, R. Johnson, C. King, T. Lang, M. Lee, D. Lettenmaier, R. Lobato, V. Magaña, J. Meiten, K. Mo, S. Nesbitt, F. Ocampo-Torres, E. Pytlak, P. Rogers, S. Rutledge, J. Schemm, S. Schubert, A. White, C. Williams, A. Wood, R. Zamora and C. Zhang, 2006: The NAME 2004 Field Campaign and Modeling Strategy. *Bull. Amer. Met. Soc.*, **87**, 79–94.

Houze, R. A., Jr., 1989: Observed structure of mesoscale convective systems and implications for large-scale heating. *Quart. J. Roy. Meteor. Soc.*, **115**, 425–461.

Houze, R.A. Jr., 1993: Cloud Dynamics, Academic Press, San Diego, California, 573 pp.

Houze, R. A., Jr., and E. N. Rappaport, 1984: Air motions and precipitation structure of an early summer squall line over the eastern tropical Atlantic. *J. Atmos. Sci.*, **41**, 553-574.

Hubbert, J., and V. N. Bringi, 1995: An iterative filtering technique for the analysis of copolar differential phase and Dual-frequency radar measurements. *J. Atmos. Oceanic Tech.*, **12**, 643–648.

Jameson, A. R., 1985: Microphysical interpretation of multiparameer radar measurements in rain. Part III: interpretation and measurement of propagation differential phase shift between orthogonal linear polarizations. *J. Atmos. Sci.*, **42**, 607- 614.

Johnson, R. H., 1982: Vertical motion of near-equatorial winter monsoon convection. *J. Meteor. Soc. Japan*, **60**, 682-690.

Johnson, R. H., 1984: Partitioning tropical heat and moisture budgets into cumulus and mesoscale components: Implications for cumulus parameterization. *Mon. Wea. Rev.*, **112**, 1590–1601

Joss, J. and A. Waldvogel, 1967: Ein Spektrograph fur Niederschlagstrophen mit automatischer Auswertung. *Pure Appl. Geophys.*, **68**, 240-246.

Joss, J., and A. Waldvogel, 1970: Raindrop size distribution and Doppler velocities. *Preprints, 14th Conf. on Radar Meteorology*, Tuscon, Arizona, Amer. Meteor. Soc., 153-156.

Keenan, T. D., and S. A. Rutledge, 1993: Mesoscale characteristics of monsoonal convection and associated stratiform precipitation. *Mon. Wea. Rev.*, **121**, 352–374.

Lang, T. J., R. Cifelli, D. Lerach, L. Nelson, S. W. Nesbitt, G. Pereira, S. A. Rutledge, D. Ahijevych, and R. Carbone, 2005: Radar observations during NAME 2004. Part II: Preliminary results. *32nd Conf. on Radar Meteorology*, Albuquerque, New Mexico, Amer. Meteor. Soc., JP3J.5.

Lang, T. J., R. Cifelli, L. Nelson, S. W. Nesbitt, G. Pereira, S. A. Rutledge, D. Ahijevych, and R. Carbone, 2005: Radar observations during NAME 2004. Part I: Data products and quality control. *32nd Conf. on Radar Meteor*ology, Albuquerque, New Mexico, Amer. Meteor. Soc., JP3J.6.

Lhermitte, R. M., and D. Atlas, 1961: Precipitation motion by pulse Doppler. *Preprints, 9th Weather Radar Conf.*, Kansas City, Amer. Meteor. Soc., 218-223.

Lin, Y., R. D. Farley, and H. D. Orville, 1983: Bulk Parameterization of the Snow Field in a Cloud Model. *J. App. Meteor.*, **22**, 1065–1092.

Liu, H., and V. Chandrasekar, 2000: Classification of hydrometeors based on polarimetric radar measurements: Development of fuzzy logic and neurofuzzy systems, and in situ verification. *J. Atmos. Oceanic Tech.*, **17,** 140-164.

Locatelli, J. D., and Peter V. Hobbs, 1974: Fall speeds and masses of solid precipitation particles. *J. Geophys. Res.*, **79**, 2185-2197.

Lubin, D., J.-P. Chen, P. Pilewski, V. Ramanathan, and F. P. J. Valero, 1996: Microphysical examination of excess cloud absorption in the tropical atmosphere. *J. Geophys. Res.*, **101**, 16961–16972.

Matejka, T., and R. C. Srivastava, 1991: An improved version of the extended velocity-azimuth display analysis of single-Doppler radar data. *J. Atmos. Oceanic Tech.*, **8**, 453–466.

May, P. T., and T. D. Keenan, 2005: Evaluation of microphysical retrievals from polarimetric radar with wind profiler data. *J. App. Meteor.*, **44**, 827–838.

Pruppacher, H. R. and K. V. Beard, 1970: A wind tunnel investigation of the internal circulation and shape of water drops falling at terminal velocity in air. *Quart. J. Roy. Meteor. Soc.*, **96**, 247-256.

Rinehart, R. E., 2004: Radar for Meteorologists, 4th Ed., Rinehart Publications, Columbia, Missouri, 482 pp.

Rogers, R. R., 1964: An extension of the Z-R relation for Doppler radar. *Preprints, 11th Conference on Radar Meteorology*, Boulder, Colorado, Amer. Meteor. Soc., 158-161.

Rutledge, S. A., R. A. Houze Jr., M. I. Biggerstaff, and T. Matejka, 1988: The Oklahoma–Kansas mesoscale convective system of 10–11 June 1985: Precipitation structure and single-Doppler radar analysis. *Mon. Wea. Rev.*, **116**, 1409–1430.

Smull, B. F., and R. A. Houze Jr., 1987: Dual-Doppler radar analysis of a midlatitude squall line with a trailing region of stratiform rain. *J. Atmos. Sci.*, **44**, 2128-2148.

Srivastava, R. C., T.J. Matejka, and T.J. Lorello, 1986: Doppler radar study of the trailing anvil region associated with a squall line. *J. Atmos. Sci.*, **43**, 356–377.

Steiner, M., R. A. Houze Jr., and S. E. Yuter, 1995: Climatological characterization of three-dimensional storm structure from operational radar and rain gauge data. *J. Appl. Meteor.*, **34**, 1978–2007.

Ulbrich, C. W., 1977: Doppler radar relationships for hail at vertical incidence. *J.App. Meteor.*, **16**, 1349–1359.

Wallace, J. M., and P. V. Hobbs, 1997: Atmospheric Science- An Introductory Survey, Academic Press, New York, New York, 467 pp.

Williams, C. R., W. L. Ecklund, and K. S. Gage, 1995: Classification of precipitating clouds in the tropics using 915-MHz wind profilers. *J. Atmos. and Oceanic Tech.*, **12**, 996–1012.

Williams, C. R., A. B. White, K. S. Gage, and F. M. Ralph, 2006: Vertical structure of precipitation and related microphysics observed by NOAA profilers and TRMM during NAME 2004. *J. Climate*, submitted.

Yanai, M., S. Esbensen, and J. H. Chu, 1973: Determination of bulk properties of tropical cloud clusters from large-scale heat and moisture budgets. *J. Atmos. Sci.*, **30,** 611–627.

Yuter, S. E., and R. A. Houze Jr., 1993: Three-dimensional kinematic and microphysical evolution of Florida cumulonimbus. *Preprints, 26th Int. Conf. Radar Meteorology*, Norman, Oklahoma, Amer. Meteor. Soc., 176-179.

Yuter, S. E., and R. A. Houze Jr., 1995: Three-dimensional kinematic and microphysical evolution of Florida cumulonimbus. Part II: Frequency distributions of vertical velocity, reflectivity, and differential reflectivity. *Mon. Wea. Rev.*, **123**, 1941-1963.

Zrnić, D.S., A. Ryzhkov, J. Straka, Y. Liu, and J. Vivekanandan, 2001: Testing a procedure for automatic classification of hydrometeor types. *J. Atmos. Oceanic Tech.*, **18**, 892-913.

Zrnić, D.S., N. Balakrishnan, C.L. Ziegler, V.N. Bringi, K. Aydin, and T. Matejka, 1993b: Polarimetric signatures in the stratiform region of a mesoscale convective system. *J. Appl. Meteor.*, **32**, 678-693.